Princeton Plasma Physics Laboratory

PPPL-

PPPL-
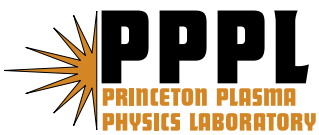
PPPL
PRINCETON PLASMA
PHYSICS LABORATORY

Princeton Plasma Physics Laboratory
Report Disclaimers

Full Legal Disclaimer

This report was prepared as an account of work sponsored by an agency of the United States Government. Neither the United States Government nor any agency thereof, nor any of their employees, nor any of their contractors, subcontractors or their employees, makes any warranty, express or implied, or assumes any legal liability or responsibility for the accuracy, completeness, or any third party's use or the results of such use of any information, apparatus, product, or process disclosed, or represents that its use would not infringe privately owned rights. Reference herein to any specific commercial product, process, or service by trade name, trademark, manufacturer, or otherwise, does not necessarily constitute or imply its endorsement, recommendation, or favoring by the United States Government or any agency thereof or its contractors or subcontractors. The views and opinions of authors expressed herein do not necessarily state or reflect those of the United States Government or any agency thereof.

Trademark Disclaimer

Reference herein to any specific commercial product, process, or service by trade name, trademark, manufacturer, or otherwise, does not necessarily constitute or imply its endorsement, recommendation, or favoring by the United States Government or any agency thereof or its contractors or subcontractors.

PPPL Report Availability

Princeton Plasma Physics Laboratory:

http://www.pppl.gov/techreports.cfm

Office of Scientific and Technical Information (OSTI):

http://www.osti.gov/bridge

Related Links:

U.S. Department of Energy

Office of Scientific and Technical Information

Fusion Links

Experimental study of the Hall effect and electron diffusion region during magnetic reconnection in a laboratory plasma

Yang Ren*, Masaaki Yamada, Hantao Ji, Seth Dorfman, Stefan Gerhardt, Russel Kulsrud

Center for Magnetic Self-organization in Laboratory and Astrophysical Plasmas,

Princeton Plasma Physics Laboratory,

Princeton University,

Princeton New Jersey 08543

Abstract

The Hall effect during magnetic reconnection without an external guide field has been extensively studied in the laboratory plasma of the Magnetic Reconnection Experiment (MRX) [Yamada *et al.*, Phys. Plasmas 4, 1936 (1997)] by measuring its key signature, an out-of-plane quadrupole magnetic field, with magnetic probe arrays whose spatial resolution is on the order of the electron skin depth. The in-plane electron flow is deduced from out-of-plane magnetic field measurements. The measured in-plane electron flow and numerical results are in good agreement. The electron diffusion region is identified by measuring the electron outflow channel. The width of the electron diffusion region scales with the electron skin depth ($\sim 8c/\omega_{pe}$) and the peak electron outflow velocity scales with the electron Alfvén velocity ($\sim 0.11V_{eA}$), independent of ion mass. The measured width of the electron diffusion region is much wider and the observed electron outflow is much slower than those obtained in 2D numerical simulations. It is found that the classical and anomalous dissipation present in the experiment can broaden the electron diffusion region and slow the electron outflow. As a consequence, the electron outflow flux remain consistent with numerical simulations. The ions, as measured by a Mach probe, have a much wider outflow channel than the electrons, and their outflow is much slower than the electron outflow everywhere in the electron diffusion region.

PACS numbers: Valid PACS appear here

---

* Present address: University of Wisconsin-Madison, 53706

I. INTRODUCTION

Magnetic reconnection is a process to convert magnetic energy to plasma kinetic and thermal energy. In the situations where magnetic energy is abundant, explosive phenomena such as magnetospheric substorms and solar flares are thought to be driven by this dynamical process [1, 2]. Magnetic reconnection also plays an important role in determining the relaxation, stability and transport properties of laboratory fusion plasmas [3–6]. This process involves the breaking and reconnecting of magnetic field lines in a narrow "diffusion region" where the ideal plasma "frozen-in" condition is violated. The diffusion region, like a throttle, controls how fast plasma can flow through and thus determines the magnetic energy release rate. An early model of magnetic reconnection, proposed by Sweet [2] and Parker [7] based on resistive magnetohydrodynamics (MHD), failed to explain the observed fast magnetic energy releasing events like solar flare and magnetic substorms. The predicted diffusion region where the plasma is detached from field lines in this MHD model is so narrow and elongated in collisionless plasma that it limits the plasma outflow flux and thus slows down the reconnection process. Petschek's model [8], by shrinking the length of the diffusion region and including slow mode shocks, can produce a faster reconnection rate, but this model has been found to be incompatible with uniform resistivity [9, 10]. It is therefore necessary to go beyond resistive MHD physics to find fast reconnection mechanisms.

Recent numerical simulations have shown that fast reconnection is facilitated by the Hall effect which is caused by decoupling of ions from the magnetized electrons in the current sheet [11–14]. The Hall effect leads to the formation of a two-scale structure in the reconnection region, an electron diffusion region embedded in a much broader ion diffusion region. According to recent 2-D numerical simulations [14–16], the width of the electron diffusion region is on the order of the electron skin depth, while the ion diffusion region is much wider, allowing the ions to flow out efficiently. In symmetric magnetic reconnection [66] having no external guide field (applied constant magnetic field perpendicular to the reconnecting plane), a key signature of the Hall effect, a quadrupole out-of-plane magnetic field, has been observed in laboratory plasmas [20–22], while it was previously indicated by satellites passing one side of the X-line [17–19] (We note that the presence of the quadrupole field is not a necessary condition for the Hall effect in an asymmetric reconnection, where the reconnecting magnetic field and plasma density are very different on two sides of the neutral

sheet, as pointed out in Ref. [23]). Furthermore, the direct observation of the decoupling of the ions and electrons, thus forming the ion diffusion region, was observed in space [23]. The electron diffusion region has also been observed in space [24–29], where it was identified by examining the violation of the frozen-in condition for the electrons or by the observation of parallel electric fields. Previously reported electron diffusion regions in laboratory were either in electron magnetohydrodynamics (EMHD) plasmas where the ions were globally demagnetized [30] or in the presence of a strong guide field which magnetized the electrons [31].

Recent research on the Magnetic Reconnection Experiment (MRX) has focused on the Hall effect and formation of the electron diffusion region [20, 21, 32, 33] during magnetic reconnection without an externally applied guide field. In the most recent paper [33], the observation of an electron diffusion region with quite different width and length than what is obtained in numerical simulations [15, 16, 34, 35] is reported. In this paper, we extend our research beyond Yamada et al.'s 2006 paper and Ref. [33], and present a more detailed study of the Hall effect during magnetic reconnection and the formation of the electron diffusion region in the laboratory plasma of the Magnetic Reconnection Experiment (MRX). The Hall effect is studied by measuring its key signature, the quadrupole out-of-plane magnetic field, with five arrays of magnetic pickup coils with resolution up to the electron skin depth in MRX ($\sim$ 1-2 mm). The in-plane current density calculated from the measured out-of-plane field, together with our density measurements with Langmuir probes, provides us with the in-plane electron flow velocity, if the ion flow can be ignored (the justification of this approximation will be discussed later in the paper). The measurement of the electron in-plane flow helps us understand the electron dynamics in the diffusion region and study the roles of the Hall effect in magnetic reconnection. The electron inflow and outflow speeds are sub-Alfvénic and super-Alfvénic respectively, consistent with numerical simulations [15, 34]. The measured electron flow leads us to identify the long-predicted electron diffusion region. We find that the width of the electron diffusion region is proportional to the electron skin depth, in agreement with numerical simulation prediction, but the absolute width is about 5 times larger than numerical results [15, 16, 34–36]. As a result, the peak electron outflow velocity, although super-Alfvénic and scaling with the electron Alfvén velocity, is still much slower than what was observed in numerical simulations [15, 37]. We found that the classical and anomalous dissipations present the MRX diffusion region, which has been

3

studied extensively [38–40], can broaden the electron diffusion region and slow the electron outflow. In addition to the electron dynamics, we also measured the ion outflow velocity with a Mach probe. This measurement demonstrates that the ion flow is much slower than the electron flow in the diffusion region, justifying our previous assumption that the in-plane currents are carried mostly by the electrons. We also find that the ions have a much broader outflow channel than the electrons, showing that the ions are demagnetized on a larger spatial scale than the electrons, supporting our identification of the electron diffusion region. Thus we are finally able to demonstrate the two-scale structure of the diffusion region long-predicted in the literature, and we find that this structure depends on the dissipation mechanism which demagnetizes the electrons. Thus, we identified the small electron diffusion region, where field line breaking occurs, in the center of the ion diffusion region in non-guide field reconnection as predicted by many 2-D numerical simulations [15, 16, 34, 36]. To our knowledge, the direct demonstration of the decoupling of electrons from ions and the formation of a demagnetized electron diffusion region in laboratory neutral sheet has not been reported in the literature prior to this work, and the roles of the Hall effect in magnetic reconnection have not been previously studied experimentally.

The paper is organized as follows. We show our experimental setup in section II. The measurements of the quadrupole magnetic field (QF) are presented in section III. We compare the properties of the QF with a theoretical model and a numerical simulation in section IV. The electron and ion dynamics are presented in section V. In this section, we show the identification of the electron diffusion region and present its properties. In section VI, we use a simple one-dimensional model to explain the observed electron outflow velocity. We will discuss the result and conclude in section VII.

II.   EXPERIMENTAL SETUP

In the MRX plasmas, the MHD criteria ($S >> 1$, $\rho_i << L$, where S is the Lundquist number; ρ_i is the ion gyroradius; L is the system scale length) are satisfied in the bulk of the plasma [41]. Figure 1 shows a cross section of the MRX vacuum vessel in a R-Z plane; the positive toroidal direction points into the plane. The initial overall geometry of the device is axisymmetric and therefore global 2D geometry is ensured. In MRX, two toroidal plasmas with annular cross sections are formed inductively around two flux cores (donut-
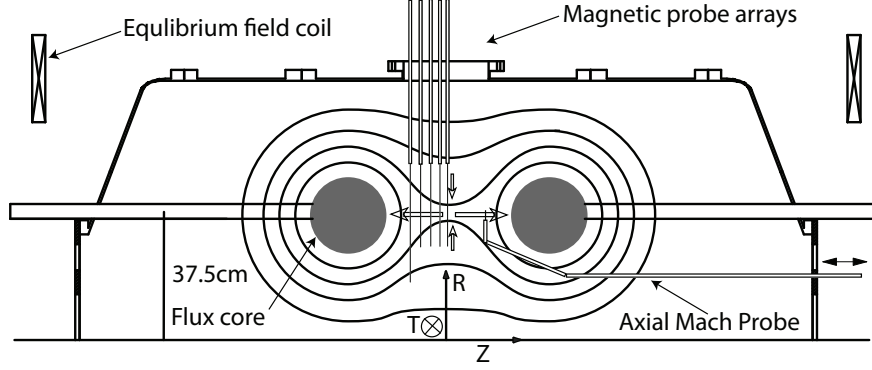
FIG. 1: Cross-sectional view of the MRX vacuum vessel. Two diagnostics, the magnetic probe arrays and axial Mach probe, are shown.
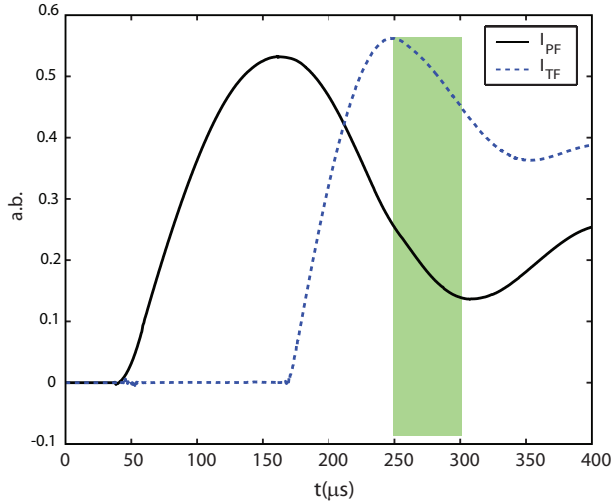
FIG. 2: (Color online) Typical poloidal and toroidal coil current waveforms. The green shaded area shows the duration when reconnection proceeds.

shaped devices with poloidal and toroidal windings inside to generate poloidal magnetic field and plasma [41, 42]). By simultaneously reducing the toroidal current in both flux cores, magnetic flux is pulled towards the flux cores, forming a current sheet and inducing magnetic reconnection. Figure 2 shows the typical PF and TF coil current waveforms used in the experiment, where PF coil is energized first to produce a vacuum poloidal field and TF coil is energized later to inductively produce plasma around two flux cores. The experimental observation of the QF has been reported in a previous paper [20] where it was measured by using a 90-channel probe array with a coarse resolution of 4 cm in both the R and Z

directions. Although the resolution in the R direction is enhanced by radially scanning the probe and averaging over many discharges, the procedure depends on the reproducibility of plasmas. Furthermore, small scale features (with spatial scale less than 1 cm) of the magnetic field profile cannot be resolved. Therefore, it is very desirable that magnetic probe arrays with high spatial resolution be used to measure the magnetic field profile. Five one-dimensional magnetic probe arrays, as shown in Fig. 1, are used to measure the profile of the out-of-plane magnetic field in the R-Z plane with a spatial resolution up to 2.5 mm in the R direction and 3 cm in the Z direction. We note that the configuration of the probe arrays can be changed to cover a wider spatial range but with a coarser resolution. A particular configuration is discussed in the next section where the QF is observed in its full extent. The in-plane current, $\mathbf{j}_{in}$, can be calculated from the out-of-plane magnetic field measurement using Ampere's law. We obtain the in-plane electron flow, $\mathbf{V}_{e,in}$, from $\mathbf{V}_{e,in} \approx -\mathbf{j}_{in}/(en_e)$, assuming that $|\mathbf{V}_i| \ll |\mathbf{V}_e|$. An axial Mach probe, which can be scanned in both the R and Z directions, is used to measure the ion outflow velocity, V_{iZ}. The plasma temperature and density are measured by two Langmuir probes (not shown). One of them is inserted radially and located at $Z = 0$. The other probe is inserted axially, like the Mach probe, and can be moved in the Z direction.

III. EXPERIMENTAL OBSERVATION OF THE QUADRUPOLE OUT-OF-PLANE MAGNETIC FIELD (QF)

The QF is verified by placing the linear magnetic probe arrays at different Z locations with the following configuration. Three linear arrays measuring the out-of-plane magnetic field were placed at $Z = -12cm$, -6 cm and 8 cm respectively. A linear array which can measure both the out-of-plane and reconnecting fields was placed at $Z = 0$ cm.

Figure 3 shows a snapshot of the radial profiles of the magnetic field measured by the fine magnetic probe arrays. The current sheet width and location can be easily identified through the reversal of the reconnecting magnetic field. The radial profiles of the out-of-plane magnetic field at $Z = -6$ cm (blue filled circles) and $Z = 8$ cm (purple filled squares) clearly show that the amplitude of the out-of-plane magnetic field is small outside of the current sheet, peaks at the current sheet edge and changes sign at the current sheet center (R≈37 cm). The QF changes from positive to negative from small radius to large radius at
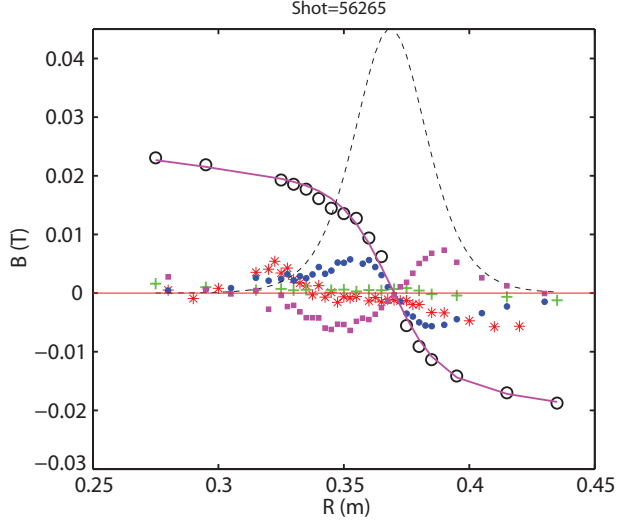
FIG. 3: (Color online) Radial magnetic field profiles at different Z positions measured by fine magnetic probe arrays in a Deuterium plasma (fill pressure=2 mTorr): the out-of-plane magnetic field B_Ts at $Z = -12$ cm (red asterisks), -6 cm (blue filled circles), 0 cm (green cross) and 8 cm (purple filled squares); and the reconnecting magnetic field B_Z (black open circles) at $Z = 0$ cm with the corresponding hyperbolic tangent fitting (solid line). The current sheet profile (dashed line, not to scale) derived from the hyperbolic tangent fitting [Yamada *et al.*, Phys. Plasmas 7, 1781 (2000)] is also shown.

$Z = -6$ cm and vice versa for the out-of-plane field at $Z = 8$ cm. At the same time, there is no (or small, around the sensitivity of the probe which is about 5 Gauss) out-of-plane magnetic field measured at $Z = 0$ cm. This is consistent with the quadrupole configuration of the out-of-plane magnetic field. The out-of-plane field at $Z = -12$ cm reverses sign at the current sheet center, but the amplitude is much smaller, indicating that the spatial extent of the QF away from the current sheet center plane ($Z = 0$ cm) in the R direction is about 12 cm. Note that the flux core surfaces in the experiment are 20 cm away from the X-line ($Z = 0$ cm). This spatial extent of the QF may be influenced by the presence of the flux cores. The effects of the flux cores on the QF will be discussed later. The measured amplitude of the QF is about 60 Gauss, and the reconnecting magnetic field has an averaged shoulder amplitude of 130 Gauss (the shoulder value of the reconnecting magnetic field is defined as the magnetic field strength at the point where the current density calculated from the hyperbolic tangent decreases to 0.42 of its peak value and the average is taken using the

7
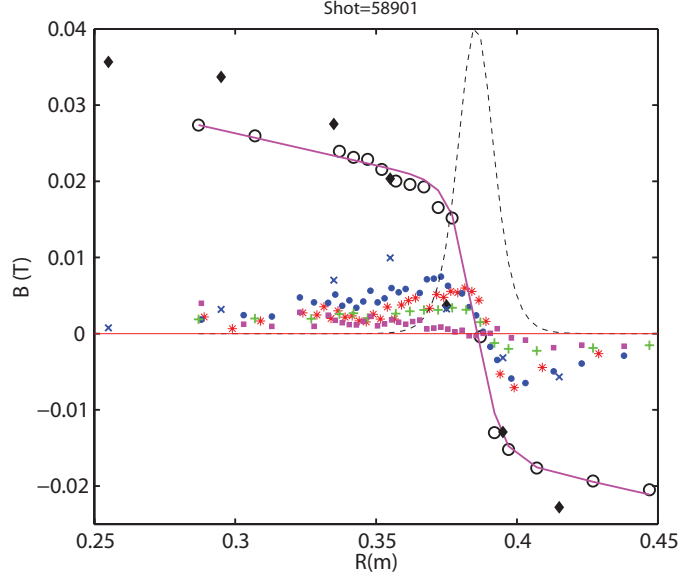
FIG. 4: (Color online) Radial magnetic field profiles at different Z positions measured by linear magnetic probe arrays in a Hydrogen plasma (fill pressure=3 mTorr): the out-of-plane magnetic field B_Ts at $Z = -12$ cm (blue x's), -9 cm (blue filled circles), -6 cm (red asterisks), -3 cm (green crosses) and 0 cm (purple filled square); and the reconnecting magnetic field B_Zs at $Z = -12$ (black filled diamonds) and at $Z = -3$ cm (black open circles) with the corresponding hyperbolic tangent fitting (solid line) at $Z = -3$ cm. The current sheet profile (dashed line, not to scale) derived from the hyperbolic tangent fitting is also shown.

values at both shoulders). This gives a ratio of 0.46 between the amplitudes of the QF and reconnecting magnetic field.

A configuration of the fine magnetic probe arrays, as shown in Fig. 1, allows unprecedented high resolution measurement of the QF in a reconnecting current sheet. Figure 4 shows a snap shot of the radial profiles of the out-of-plane toroidal field B_T at $Z = 0$, -3, -6, -9 and -12 cm, and the reconnection field B_Z and out-of-plane current density profile j_T at $Z = -3$ cm. The snap shot is taken at a time well after reconnection begins. In the figure, the out-of-plane magnetic fields at $Z = -9$ cm and $Z = -3$ cm reverse sign around the current sheet center ($R = 37.5$ cm). The out-of-plane magnetic field at $Z = 0$ does not reverse sign in the current sheet center, confirming the quadrupole configuration of the out-of-plane magnetic field. Some residual out-of-plane magnetic field can be seen at $Z = 0$ cm outside of the current sheet. This residual field has an amplitude of 20 Gauss

8

which is much smaller than the reconnecting magnetic field (~ 200 Gauss). This field is leftover from the initial out-of-plane (toroidal) magnetic field produced during the plasma generation process. The amplitude of the QF in the figure is about 80 Gauss. The ratio between the amplitude of the out-of-plane magnetic field B_T and reconnection magnetic field B_Z (using the averaged shoulder value) reaches 0.6, showing that a substantial amount of QF can be generated during magnetic reconnection. Note that the distance between the maximum and the minimum of the out-of-plane magnetic field in the R direction is the narrowest at $Z = -6$ cm, which means the in-plane current density peaks here (the amplitude of the out-of-plane magnetic field here is close to its maximum value in the R-Z plane). It may be assumed that the electrons carry most of the current, and the measured density profile in the Z direction remains flat up to $Z = -6$ cm (not shown). This means that the electrons have the maximum outflow velocity at $Z = -6$ cm. Thus at $Z > -6$ cm, electrons are accelerated, and at $Z < -6$ cm electrons are decelerated. The measurement of the out-of-plane magnetic field provides an opportunity to study the electron dynamics in the current sheet. This will be discussed in detail in Section V.

A. Temporal Characteristics of the QF

Figure 5 shows an example of the time evolution of the out-of-plane magnetic field during magnetic reconnection in MRX. The color-coded contours show the out-of-plane magnetic field (B_T) strength (in Tesla). The arrows show $-\mathbf{j}_{in}$, where $\mathbf{j}_{in}$ is the in-plane current density associated with the out-of-plane magnetic field calculated from Ampere's law. The thick white line shows the current sheet center position inferred from the measurement of the reconnecting magnetic field. Throughout the four panels, it can been seen that the reversal position of the QF is always coincident with the current sheet center. This is exactly how the QF was observed in numerical simulations: the electron outflow must be aligned with the current sheet center and the associated current produces the QF.

At $t = 281.2$ μs (upper-left panel), a strong out-of-plane magnetic field (deep blue color, about -100 Gauss) above the current sheet center, and a weaker out-of-plane field with opposite sign (light yellow color about 20 Gauss) below the current sheet center can be seen. The strong out-of-plane magnetic field is the initial out-of-plane field produced by the the TF coil current ramping-up (see Fig. 2). The weaker out-of-plane magnetic field is produced
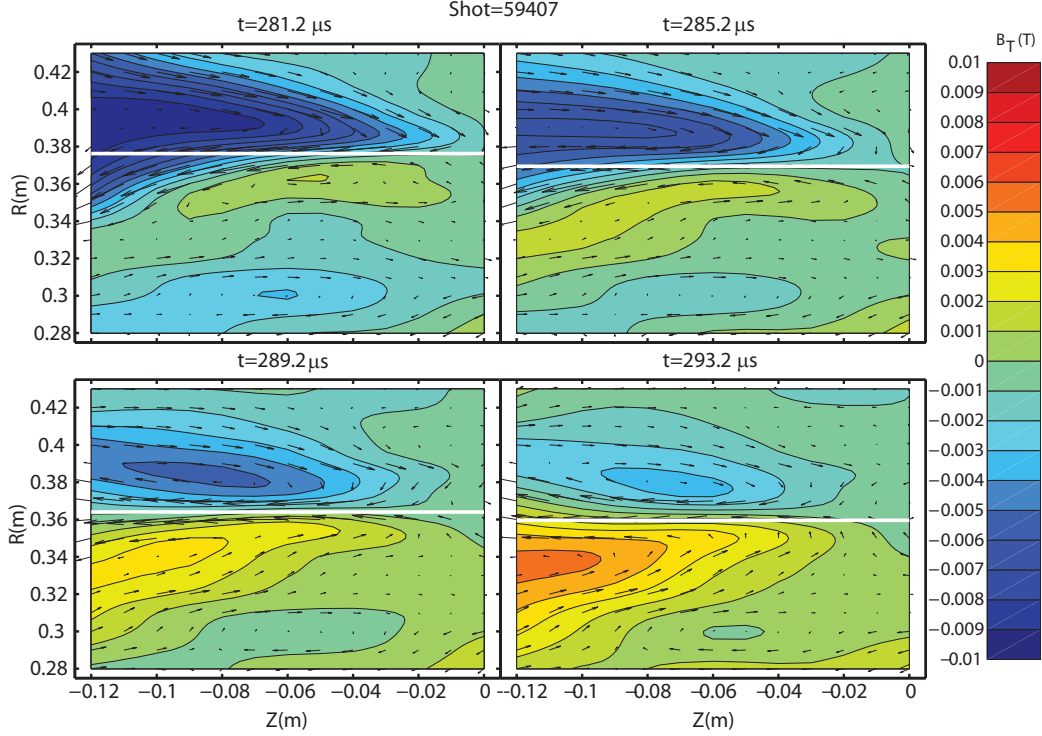
FIG. 5: (Color) The time evolution of the out-of-plane magnetic field during magnetic reconnection at t=281.2 μs, 285.2 μs, 289.2 μs and 293.2 μs measured using five linear magnetic probe arrays at Z=-12 cm, -9 cm, -6 cm, -3 cm and 0 cm in a Hydrogen plasma (fill pressure=2 mTorr). The color-coded contour shows the out-of-plane magnetic field strength; the arrows show $-\mathbf{j}_{in}$, where $\mathbf{j}_{in}$ is the in-plane current density; and the thick white line shows the current sheet center position.

because the out-of-plane electron flow is pulling the in-plane magnetic field into the plane. This pulling process weakens the initial magnetic field and produces positive out-of-plane field below the current sheet center. The upper-right panel shows the profile of the out-of-plane magnetic field 4 μs later; the positive out-of-plane field below the current sheet center becomes stronger and broader, as the initial out-of-plane field is further weakened.

At $t = 289.2$ μs, another 4 μs later, shown in the lower-left panel, the positive and negative out-of-plane magnetic field becomes symmetric in terms of maximum strength (40 Gauss vs. 50 Gauss) and spatial extent in the R direction. Around this time, the QF is fully developed and the influence of the initial out-of-plane magnetic field is gone. It is around this time that the characteristics of the QF are studied throughout this paper.

At $t = 293.2$ μs, as shown in the lower-right panel, the positive out-of-plane field becomes

stronger and the negative out-of-plane field is weakened. This is because the out-of-plane magnetic field is driven by the inductive electric field from the TF coil current ringing (after increasing it decreases; see Fig. 2). When the TF coil currents increase, the inductive electric field produces the negative out-of-plane magnetic field shown in upper-left panel. As the TF coil currents start to decrease, the inductive electric field changes sign and produces positive out-of-plane magnetic field. This newly produced out-of-plane field does not have the quadrupole-type configuration, and its effect is to weaken the negative out-of-plane field and to enhance the positive out-of-plane field as shown in the lower-right panel. Eventually the QF would disappear because of this effect (not shown), but this time is already at end of the reconnection process (this is when the plasma current and reconnecting electric field start to decay quickly), and does not affect our analysis on the QF. Note that the QF in this discharge lasts for about 12 Alfvén times.

Because of the coupling between the out-of-plane field and the TF coil current, one may ask if the quadrupole-type configuration in the out-of-plane field is driven by the inductive electric field from the TF coil current ringing. By examining the upper-right panel in Fig. 5, this question can be answered. If the positive out-of-plane field were produced around the flux cores and then were carried by plasma or diffused to the center, then we should have seen that positive out-of-plane field being injected into the experimental observation area from the boundary ($Z = -12$ cm). On the contrary, the panel shows that the positive out-of-plane field is first produced around R∼34 cm and Z∼-6 cm. This can only be explained if local plasma current, not driven by the inductive electric field from the TF coil currents, produces the field. Thus this is an effect due to the reconnection dynamics, the Hall effect, and is not driven by the TF coil current.

The effect of the TF polarity has been studied by changing the TF coil connection. The initial toroidal fields produced around the flux cores then have different signs (positive at Z<0 and negative at $Z > 0$) than before the change (negative at Z<0 and positive at $Z > 0$). This change does not affect either the sign of the QF or the reconnection process itself.

Finally, we note that the generation of the QF in MRX requires the initial out-of-plane magnetic fields around the two flux cores from the plasma generation process to cancel each other nicely. Otherwise the residual out-of-plane field can mask the QF. If it is too large (comparable to reconnecting magnetic field), it can even prevent the generation of the QF [43]. Thus, carefully selecting the experimental conditions is the key for producing

the QF. These conditions include the flux core distance, Z_0, and the charging voltages of capacitor banks. we note that even with the best selection of experimental conditions, the generation of the QF is not guaranteed in every discharge; only about 50 percent of the discharges develop the QF, although reconnection occurs in every shot. Note that this is similar to space observation, where the QF is only observed in a fraction of reconnection events [44]. The shot-to-shot variation is likely due to the different initial conditions of the out-of-plane magnetic fields in each discharge as discussed above. The analysis presented in the manuscript is based on an ensemble of discharges which display the QF, selected from a larger number of discharges. This selection is necessary to ensure that all discharges have 2D Hall-mediated reconnection and have no guide field, i.e. the QF is present. We note that within the ensemble of discharge selected, the reproducibility is good, which allowed us to measure the quadrupole field reported in a previous paper [20].

IV. COMPARISONS WITH THEORETICAL MODELS

The observed QF as shown in the previous section is consistent with the original picture proposed by Sonnerup [45]. In this section, comparisons with a more refined theoretical model and a numerical simulation are presented.

A. Comparison with the Uzdensky-Kulsrud Model

A simple model of the physical origin of the QF was discussed in a recent paper [46]. The main idea of the model is that the expansion (shrinking) of flux tubes, as they move toward (away from) the X-line, results in a small charge separation, so that electrons are drawn toward (away from) the X-line. These in-plane motions produce an out-of-plane magnetic field with a quadrupole pattern around the separatrices. This quadrupole field is proportional to a quantity called the volume-per-flux integral which is controlled by the in-plane magnetic field structure. Here we compare the results from the model with those from the experiments.
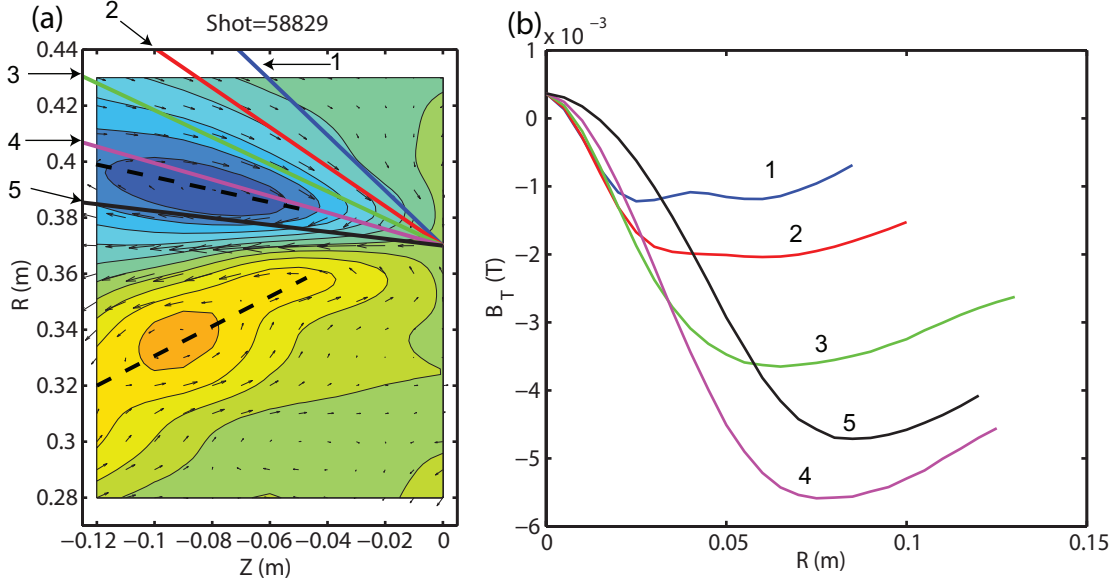
FIG. 6: (Color online) The out-of-plane magnetic fields on straight rays from the X-line: (a) The two-dimensional profile of the QF in a Hydrogen plasma (fill pressure=2 mTorr). The thick color-coded solid lines show the positions of the straight rays ($1 \rightarrow 45°$, $2 \rightarrow 55°$, $3 \rightarrow 64°$, $4 \rightarrow 74°$, $5 \rightarrow 83°$) and the thick black dashed lines denote the position of the separatrices inferred from the ridges of the QF [M. Yamada *et al.*, Phys. Plasmas 13, 052119 (2006)]. (b) The out-of-plane magnetic field strength on the straight rays with colors and numbering corresponding to the lines in (a).

1. Comparisons with the X-type Diffusion Region

In Ref. [46], an X-line type diffusion region is used to derive an analytical expression for the electron flow and the quadrupole field. It is shown that the electrons flow along straight rays towards the X-line, and the quadrupole field strength is a constant along the rays pointing away from the X-line. We can test this simple picture by comparing it with the experiment.

Figure 6(a) plots the color-coded contours of the out-of-plane magnetic field in the R-Z plane. The left half of the QF can be clearly seen. The rays on which the out-of-plane field is evaluated are drawn as thick lines in colors: blue, red, green, magenta and black. At the angles of 45, 55, 64, 74, 83 degrees with the positive Z-axis respectively. Figure 6(b) plots the out-of-plane magnetic field strength along each ray drawn in (a) using the same color coding

13

and numbering. One interesting feature is that the out-of-plane field strength increases as we move away from the X-line ($r = 0$ cm), and then tends to saturate, where r denotes the distance on the rays from the X-line. Taking the red line for example, we can see that the field strength increases until $r \sim 3$ cm and then stays relatively constant for a wide range of distance: $r \sim 3$ cm to $r \sim 10$ cm. The field along the magenta and black lines requires a longer distance to reach a constant amplitude. We conclude that at sufficient distance from the X-line, the out-of-plane field along a straight ray away from the X-line is approximately constant, which is in good agreement with the calculation presented in the paper [46]. Thus the simple X-type diffusion region can be a good assumption away from the X-line ($r > 2.5$ cm) and away from the separatrices where the out-of-plane field strength maximizes. The difference comes from: (1) the deviation of the in-plane field from the simple X-type configuration; (2) the breaking of the electron "frozen-in" condition. Around the X-line, the in-plane field is modified to form a quasi-one-dimensional current sheet which deviates greatly from an X-type configuration. At the same time, the electrons start to decouple from the fields. It is shown in the paper that B_Y has logarithmic singularities at the separatrices. Uzdensky and Kulsrud pointed out that these singularities can be smoothed out if electron inertia is taken into account in the generalized Ohm's law [46]. The deviation from the model around the separatrices is obvious in the measurements: since the magenta and black lines are close to a separatrix (thick black dashed line), it takes longer distance for the field along them to reach a constant amplitude.

2. Comparisons on the Field-aligned Current

Another prediction of the Uzdensky-Kulsrud model is that large scale field aligned currents should be observed in the diffusion region. This field aligned current has been observed in space observations [47] and is shown to produce the QF. In the MRX experiments, one magnetic probe array (with coil separation down to 2cm) at $Z = -12$ cm measures all three components of the magnetic field simultaneously. By combining the measurement of this probe array with fine probe array measurements, the angle between the in-plane current density and the in-plane magnetic field can be determined at $Z = -12$ cm as $\theta = \arccos(\mathbf{j}_{in} \cdot \mathbf{B}_{in}/(|\mathbf{j}_{in}||\mathbf{B}_{in}|))$, where $\mathbf{B}_{in}$ is the in-plane magnetic field. Figure 7(a) plots B_Z, B_R and B_T, indicating the magnetic field direction. B_Z and B_T change sign at the

14
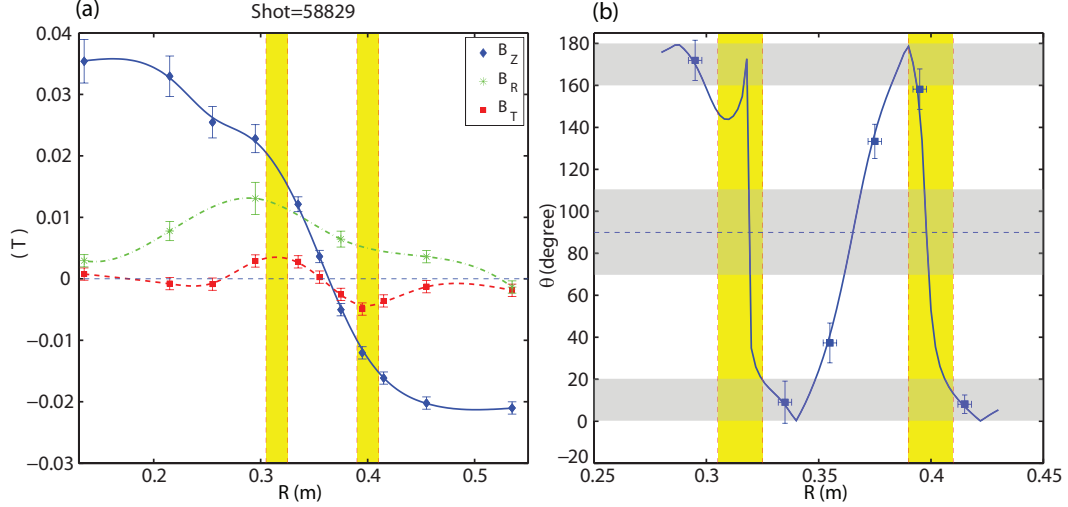
FIG. 7: (Color online) (a) The measured reconnecting magnetic field B_z (blue filled diamonds), measured B_R (green asterisks) and measured out-of-plane magnetic field B_T (red filled squares) a Hydrogen plasma (fill pressure=2 mTorr). The spline fits for B_Z, B_T and B_R are shown as the blue solid line, the green dash-dotted line and the red dashed line respectively. (b) The angle (θ) between the in-plane current density ($\mathbf{j}_{in}$) and the in-plane magnetic field ($\mathbf{B}_{in}$), $\theta = \arccos(\mathbf{j}_{in}\mathbf{B}_{in}/(|\mathbf{j}_{in}||\mathbf{B}_{in}|))$, is calculated from $\mathbf{B}_{in}$ at the coil positions (blue filled squares) and from the spline fits (blue solid line). The vertical yellow strips in (a) and (b) shows the region where the out-of-plane magnetic field peaks. Two horizontal dashed lines in (a) and (b) are for references to 0 and 90° respectively. The horizontal shaded regions in (b) indicate the regions where the in-plane current is parallel, anti-parallel or perpendicular to the in-plane magnetic field as defined in the text.

same position while B_R remains positive. The reversals of B_Z and B_T indicate the positions of the diffusion region and the outflow region respectively. The peaks of B_T denote the positions of the separatrices [12, 21, 34, 43, 46]. The finite B_R shows that the position under study is away from the X-line. Figure 7(b) plots θ as a function of R. Let us then study how θ changes as a function of R. In order to quantify the parallelity between the in-plane current and the in-plane magnetic field, we define that if $\theta < 20°$ ($\theta > 160°$), the in-plane current is parallel (anti-parallel) to the in-plane magnetic field, and if $|\theta - 90| < 20°$, the in-plane current is perpendicular to the in-plane magnetic field. In other words, when $\theta < 20°$ ($\theta > 160°$), 94 percent of the in-plane current is flowing in parallel (anti-parallel)

to the in-plane field, and when $|\theta - 90| < 20°$, 94 percent of the in-plane current is flowing perpendicularly to the in-plane field.

Figure 7(b) shows that in the regions, $R <$0.3 m or 0.382 m $< R <$0.394 m, the in-plane current is mostly anti-parallel to the in-plane field; in the regions, 0.325 m $< R <$0.35 m or $R >$0.405, the in-plane current is mostly parallel to the in-plane field; in the regions, 0.36 m $< R <$0.37 m or 0.397 m $< R <$0.399 m or 0.318 m $< R <$0.320 m, the in-plane current is mostly perpendicular to the in-plane field. We note that the length of the region with parallel or anti-parallel in-plane current is about 8 cm out of the whole observational range about 15 cm, 53 percent of the total length. The area for the observed perpendicular current is about 1.4 cm out of 15 cm, 9 percent of the total length. Thus, in a large scale (comparing to the total observational range), the in-plane current tends to be aligned with the in-plane magnetic field. This agrees well with the prediction of the Uzdensky-Kulsrud model. It is also clear in Fig. 7(b) that the sharp transitions from anti-parallel to parallel and from parallel to anti-parallel always occur in the two vertical yellow strips (the locations of the separatrices). Since the magnetic field direction varies little in these two regions, the in-plane current must change direction sharply. This also agrees with the Uzdensky-Kulsrud model, where the electron currents change directions across the separatrices. Note that the gradual transition from anti-parallel to parallel in the center of the outflow region comes from the change of the in-plane magnetic field direction.

In the discussion above, we have only studied the angle between the in-plane current and the in-plane magnetic field. In order to study the angle between the total current and the total magnetic field, the out-of-plane current density measurement is needed. At $Z = -12$ cm, we do not have a sufficiently detailed measurement of the total current density[67]. However, in the region, $R < 0.32$ m, we have B_R and $B_Z \gg B_T$ and the out-of-plane current density is small. Then we have $j_T B_T \ll (j_R B_R + j_Z B_Z)$, indicating that the contribution from $j_T B_T$ to the total angle calculation can be neglected. Then in the region $R < 0.32$ m, the total current is also aligned with the total magnetic field. A similar argument can be applied to the region, $R > 0.405$m, where we have $B_Z \gg B_R$ and B_T. Thus, we conclude that in the regions, $R < 0.32$ m or $R > 0.405$ m, the total current is aligned well with the total magnetic field. Since the out-of-plane current cannot be neglected in the outflow region, 0.32 m $< R < 0.395$ m, measurements of the out-of-plane current density are needed to evaluate the angle between the total current and the total magnetic field at 0.32 m $< R < 0.395$ m.

B.   Comparison with a Numerical Simulation
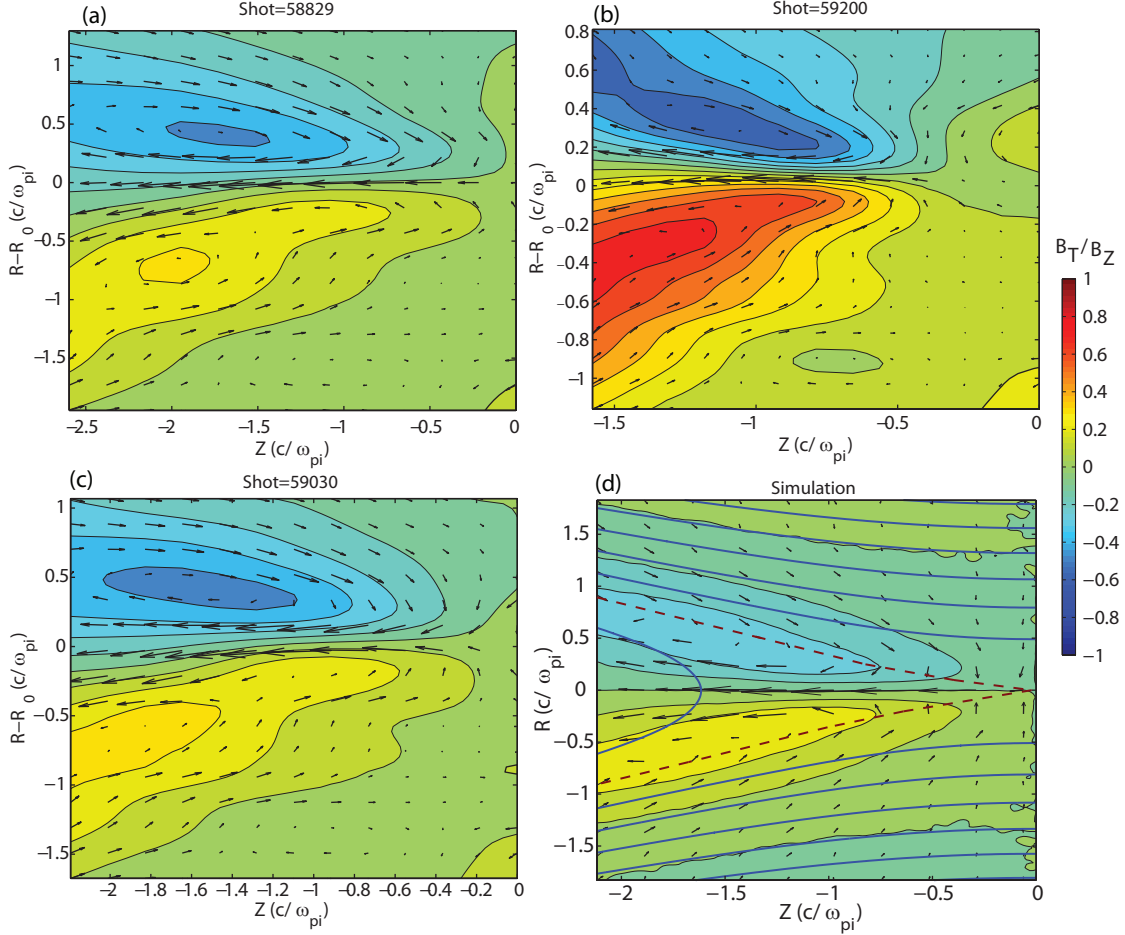
FIG. 8: (Color) Measured quadrupole out-of-plane magnetic field color-coded contours with dimensions normalized to c/ω_{pi}: (a) Hydrogen plasma (fill pressure=2 mTorr); (b) Helium plasma (fill pressure=8 mTorr); (c) Deuterium plasma (fill pressure=2 mTorr), all with the black arrows showing the in-plane electron flow velocity. (d) The QF profile (shown in color) from the numerical simulation with magnetic flux lines (solid line) and separatrices (dashed line). The current sheet center, $R = R_0$, is determined from the reconnecting magnetic field measurement, e.g. in Fig. 3 and Fig. 4.

In order to simulate the reconnection process in MRX, a fully kinetic numerical model [35] using boundary conditions similar to the experiment has been constructed utilizing the existing NPIC 2D code [16]. The simulation is conducted in a 75 cm×150 cm box, where conducting boundary conditions applied for fields and elastic reflection for particles at the

17

walls. A current carrying coils of radius 1.3 cm, contained within a larger concentric flux core of radius 9.4 cm, is placed on each side of the simulation box. The the surface-to-surface separation of two flux cores is 40 cm as in the experiment. Insulating boundary condition is applied to the flux core surface, and on the surface, particles may be absorbed or reflected depending on a reflection coefficient. As the current is ramped down according to a sinusoidal waveform modeled on the PF coil current of MRX (See Fig. 2) and reconnection is driven, both ion and electron dissipation layers are formed. The simulation is conducted with the following parameters: initial density of $2.6 \times 10^{19} \ m^{-3}$, $m_i = m_p$ (m_p is the proton mass), $m_e = m_i/75$ (m_e is the electron mass), the coil current ramp-down time scale is 200 initial ion cyclotron times, and no particle reflections at the flux core surfaces. Simulation parameters are chosen by matching the global reconnection rate and the current sheet thickness on the ion scale with experimental values in Hydrogen plasmas. Note that in order to compare the QF measured in plasmas of different ion species with that in the simulation, the dimensions in the experimental figures are normalized to c/ω_{pi}, calculated from the center density. Note that this simulation will be used for comparison in the rest of this paper.

Figure 8 plots the measured QF in Hydrogen plasma ((a)), Helium plasma ((b)), Deuterium plasma ((c)) and the QF profile from the numerical simulation. Similarities among the figures can be readily seen. The measured out-of-plane fields show clearly the quadrupole configuration, which agrees with the numerical simulation result in Fig. 8 (d). In Fig. 8 (d), we can see that the QF strength goes to zero around the X-line and increases as we move away from the X-line along the separatrices (dashed lines). The QF contours, for a large range, are in parallel with the separatrices. These contours are also the in-plane current streamlines (since the simulation is of 2D geometry). Thus, the in-plane currents, as shown in the last section, are also in parallel with the separatrices and the in-plane magnetic field lines. In Fig. 8 (a), (b), (c), the features mentioned above can be easily seen. Note that the X-line is at $Z = 0$ and $R = R_0$ for Fig. 8 (a), (c) and at $Z \approx -0.3c/\omega_{pi}$ and $R = R_0$ for Fig. 8 (b). It is more difficult to compare the positions of the measured QF and separatrices. The positions of separatrices in the experiments are not easy to identify accurately, since this requires measurements of the in-plane magnetic field with high resolution. However, the presence of the QF actually provides us with a method to identify the separatrices with the out-of-plane magnetic field measurement only.

The magnitude of the QF can be characterized by the ratio between its amplitude (the

peak value) and the upstream reconnecting magnetic field (the value at 3δ from the current sheet center, where δ is the current sheet width defined as in Ref. [40]). This ratio ranges from 30 to 60 percent in Fig. 8 (a), (b) and (c). Thus, the measured QF is on the same order of the reconnecting magnetic field. The ratio is reproduced in the simulation result shown in Fig. 8 (d). This observation is also in agreement with theoretical prediction [11], numerical simulations [34, 48] and space observations [19, 49], e.g. the ratio is 50 percent in Ref. [19].

One prominent common feature among the experimental results (Fig. 8 (a), (b), (c)) is that the QF contours tend to converge at certain Z positions, although the exact positions cannot be determined quantitatively from the contour plots. The contours then diverge, leaving a larger outflow channel for the electrons. This feature will also be explored later. We will show that the converge position of the contours corresponds to the location of the peak electron outflow velocity. The feature is also present in Fig. 8 (d).

V.   THE ROLES OF THE HALL EFFECT IN MAGNETIC RECONNECTION

The Hall effect plays important roles in reconnection. First, it introduces an electron diffusion region along with the ion diffusion region. The Hall term in the generalized Ohm's law is an term which balances the reconnecting electric field when $\mathbf{V} \times \mathbf{B}$ becomes small, *i.e.* the ions are demagnetized, and thus the ions and electrons can be demagnetized on different spatial scales. The diffusion regions of ions and electrons on different spatial scales can facilitate reconnection [14]. Second, because of the Hall effect the electron outflow velocity from the electron diffusion region is not limited by the ion Alfvén velocity and is super-Alfvénic. This property eliminates the mass flow limitation in the classical Sweet-Parker model, where the outflow velocity is limited by the ion Alfvén velocity. These roles of the Hall effect are discussed in detail in the following sections.

The observation of the most significant signature of the Hall effect in symmetric magnetic reconnection without a guide field, the QF, has been established in Section III. From the observation of the QF, both the temporal and spatial characteristics of the Hall effect and its dependence on plasma parameters can be studied to reveal the roles that the Hall effect plays in reconnection. The variation of plasma parameters (temperature and density) was accomplished mainly by changing the fill pressure of working gasses.

A. Electron In-plane Flow During Magnetic Reconnection
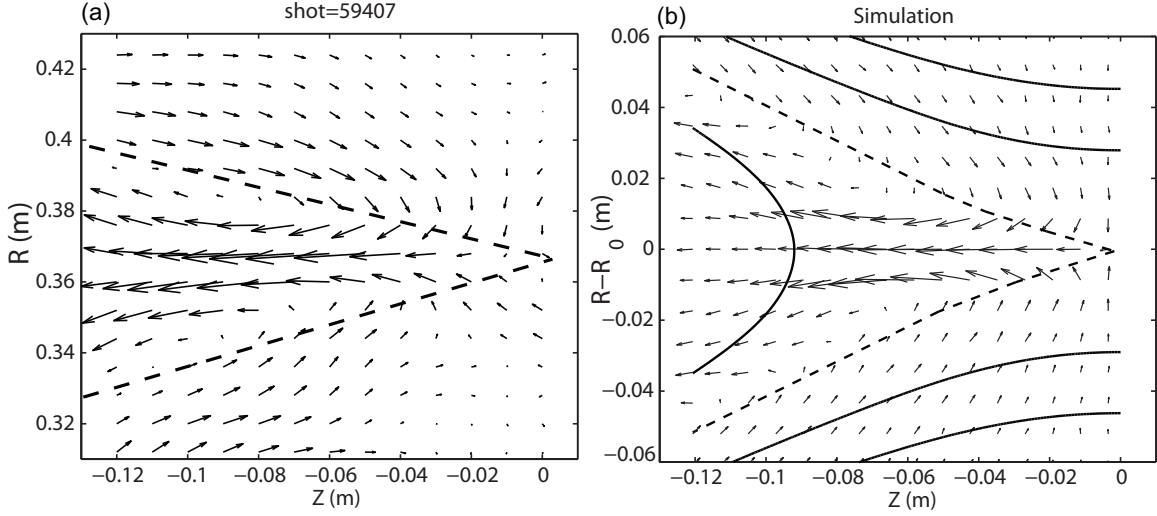
FIG. 9: (a) The in-plane drift velocity (black arrows), $\mathbf{V}_d = \mathbf{V}_e - \mathbf{V}_i$, deduced from the out-of-plane field measurement and separatrices inferred (black dashed lines) in a Hydrogen plasma (fill pressure=2 mTorr); (b) In-plane flows of electrons (black arrows), flux lines (black solid line) and separactrics (black dashed lines) from the numerical simulation.

The in-plane drift velocity, $\mathbf{V}_d = \mathbf{V}_e - \mathbf{V}_i$, can be deduced from the out-of-plane field (B_T) measurement from the Ampere's law: $\mathbf{j}_{in} = \nabla \times \mathbf{B}_T/\mu_0$. In order to deduce the in-plane electron flow, the ion flow velocity is needed. In MRX, the ion flow is measured by a Mach probe which provides a single point measurement of one component of the ion flow velocity (V_{iZ}) during each discharge. Thus mapping a 2D ion flow pattern in MRX is not realistic. However, provided that $|\mathbf{V}_d| \gg |\mathbf{V}_i|$, we can still draw conclusions about the in-plane electron flow from the drift velocity measurement. We are able to identify from Fig. 9(a) the regions where the $|\mathbf{V}_d| \gg |\mathbf{V}_i|$ condition can be satisfied, knowing that the typical ion in-flow velocity and outflow velocity are about 0.1-0.2V_A for both Hydrogen and Deuterium plasmas (see Refs. [38] and [50]). Figure 9 (a) shows the calculated in-plane drift velocity (arrows) in the R-Z plane and (b) shows the electron flow (arrows) from the numerical simulation. In Fig. 9(a), the out-flow region has $V_d \sim 2V_A$, thus the drift velocity there accurately represents the electron velocity. The region around the separatrices (black dashed lines in (a)), except for the region, $Z > -0.05$ m, has a negligible V_d, thus the ion flow cannot be neglected there. Further away from both separatrices in the inflow region,

V_d becomes large again, and can be taken as the electron flow velocity. The same condition is also satisfied in the region around the X-line, namely 0.35 m$< R <$0.39 m and $Z > -0.03$ m.

Knowing where the approximation is valid, we can then compare the electron flow pattern with that of the numerical simulation [35]. Note that Fig. 9 (b) is shown in the same physical dimensions as Fig. 9 (a). One prominent common feature, which can be readily seen, is that when the electrons come into the diffusion region, they tend to flow towards the X-line. As they approaches the separatrices, the electrons make a sharp turn and then are accelerated to about twice the ion Alfvén velocity in the outflow region.

B. The Electron Inflow and Outflow

1. The Electron Inflow
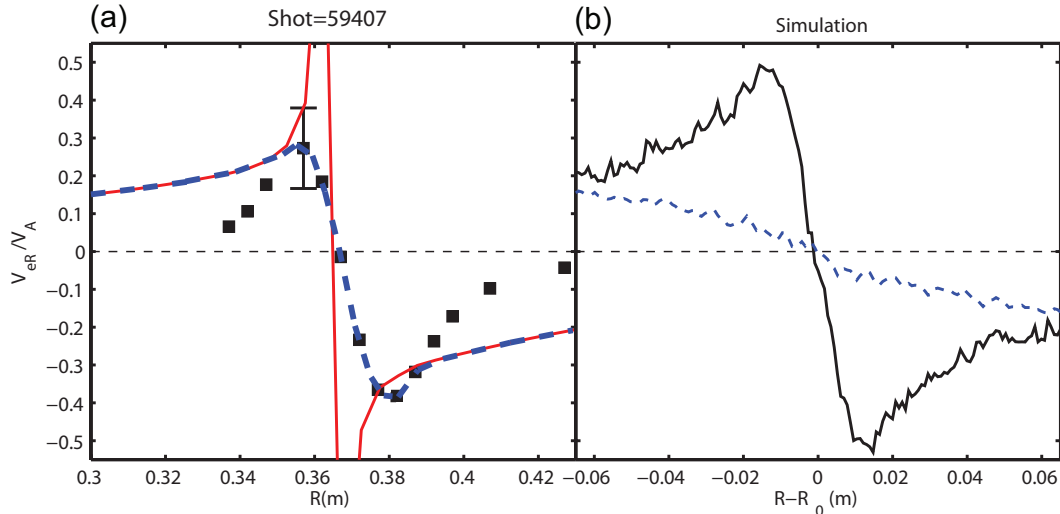
FIG. 10: (Color) (a) The radial component of the $\mathbf{E} \times \mathbf{B}$ drift (red solid line), the drift velocity $j_R/(en_e)$ (black filled squares) and the in-plane electron flow (blue dashed line) as a function of R at $Z = -3$ cm in a Hydrogen plasma (fill presssure=2 mTorr); (b) The electron inflow velocity (black solid line) and the ion inflow velocity (blue dashed line) versus R from the numerical simulation.

In Fig. 10(a), the blue dashed line shows the electron inflow (V_{eR}) normalized to the ion Alfvén velocity as a function of R at $Z = -3$ cm (i.e. 3 cm away from the X-line) [68]. The electrons flow towards the current sheet center and V_{eR} peaks about 1 cm away from the

21

current sheet center. This electron inflow velocity is deduced from both the $\mathbf{E} \times \mathbf{B}$ drift and in-plane drift velocity $j_R/(en_e)$ as follows. Well away from the diffusion center ($R < 0.33$ m or $R > 0.43$ m), the electrons and ions have the same $\mathbf{E} \times \mathbf{B}$ drift, and no in-plane current is produced, $j_R/(en_e) \approx 0$. This is the region where the in-plane current cannot be used to deduce the in-plane electron flow. Approximately 4-6 cm away from the X-line, the ions start to deviate from the $\mathbf{E} \times \mathbf{B}$ motion. On the other hand, the electrons still follow field lines, and the $\mathbf{E} \times \mathbf{B}$ drift describes the electron motion. Close to the current sheet center (0.355 m$< R < 0.38$ m), the $\mathbf{E} \times \mathbf{B}$ motion start to diverge, and is not a good description of the electron motion anymore. In this region, the ion motion is negligible and $-j_R/(en_e)$ is a good approximation to the electron flow. Thus, by combining both the $\mathbf{E} \times \mathbf{B}$ drift and in-plane drift velocity $j_R/(en_e)$, we deduced the electron inflow velocity shown as blue dashed line in Fig. 10(a). Comparing Fig. 10(a) with Fig. 10(b), we found that:

1. In Fig. 10(a), the peak electron inflow velocity is about $(0.26 - 0.38)V_A \pm 0.12V_A$, which is smaller than the peak inflow velocity (about $0.5V_A$) shown in (b). Note that the B_T measurements have a resolution of 3 cm in the Z direction and $V_{eR} \approx -\partial B_T/\partial Z/(en_e)$. Thus the measured peak V_{eR} is an average over 3 cm, and could be smaller than the peak value in the simulation. The asymmetry in the peak inflow velocity between the two inflow directions in (a) is due to the inward motion of the current sheet center in the experiment and the toroidal effect [51]. The ion inflow velocity inferred from the $\mathbf{E} \times \mathbf{B}$ drift in (a) is about 0.15-0.2V_A, in good agreement with the ion inflow velocity ($\approx 0.15V_A$) shown in (b).

2. In both Fig. 10(a) and (b), the electrons are accelerated until they approach the current sheet center to about 1 cm. They then start to deviate from the $\mathbf{E} \times \mathbf{B}$ drift. We note that the ions decouple from the electrons approximately 4-7 cm away from the current sheet center in (a), which is not only in agreement with a distance of about 6 cm in (b) but also much larger than the distance (~ 1 cm) for the electrons to decouple from the magnetic field. This illustrates that the electrons have a much narrower outflow channel than the ions, since the particles start to flow outward when they are demagnetized.

  2. *The Electron Outflow*

Figure 11(a) shows the electron outflow (V_{eZ}) normalized to the ion Alfvén velocity as a function of Z at the current sheet center. In the outflow region, as discussed in Section
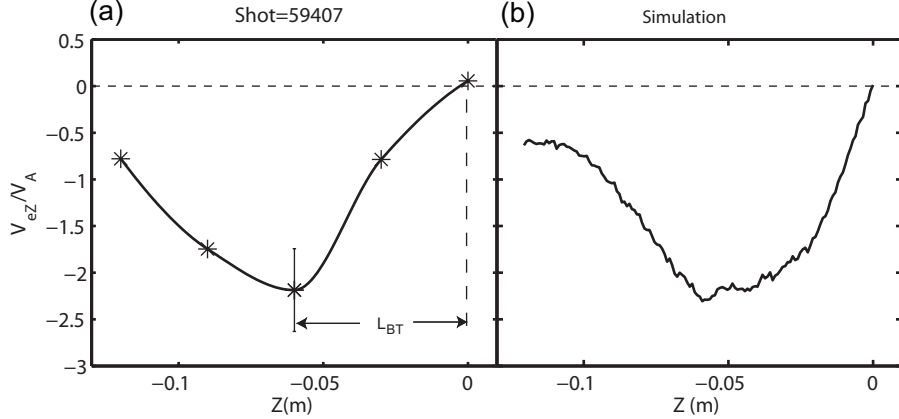
FIG. 11: Electron outflow velocity normalized to ion Alfvén velocity versus Z at the current sheet center ($R = 0.37$ m): (a) from measurement (asterisks) in a Hydrogen plasma (fill pressure=2 mTorr); (b) from the numerical simulation. The back line in (a) is the interpolation of the measurement.

V A, the in-plane drift velocity represents the electron flow velocity. It can be seen that the electron peak outflow velocity is about $2.2V_A \pm 0.5V_A$ and the distance for electrons to be accelerated to the peak velocity (L_{BT}) is about 6 cm. We note that the measured electron outflow velocity ranges from $1.5V_A$ to $4V_A$, depending on the plasma collisionality. These numbers agrees with the same quantities shown in Fig. 11(b): $2.2V_A$ and 6 cm. This good agreement, in contrast to simulations with large periodic or open boundary conditions [16], suggests that the dynamics of the electrons in the outflow direction in the experiment is reproduced in the simulation by employing MRX boundary conditions in the simulation. More details of the simulation will be reported in a separate paper [35].

The super-Alfvénic electron outflow is one of the key signatures of Hall-mediated fast magnetic reconnection [13, 15, 29, 34]. The plasma outflow in the classical Sweet-Parker model is limited by the ion Alfvén velocity. This severely limits the reconnection rate because the outflow channel shrinks substantially in the collisionless regime. The ability for the electron flow to reach super-Alfénic outflow velocities enables the electrons to flow in the narrow channel without limiting the reconnection rate. The ions, on the other hand can flow in a wider channel, as will be shown in the next section.

Finally, note that the reasonable agreement between the absolute value of the in-plane electron flow in the experiment and numerical simulations does not necessarily mean that
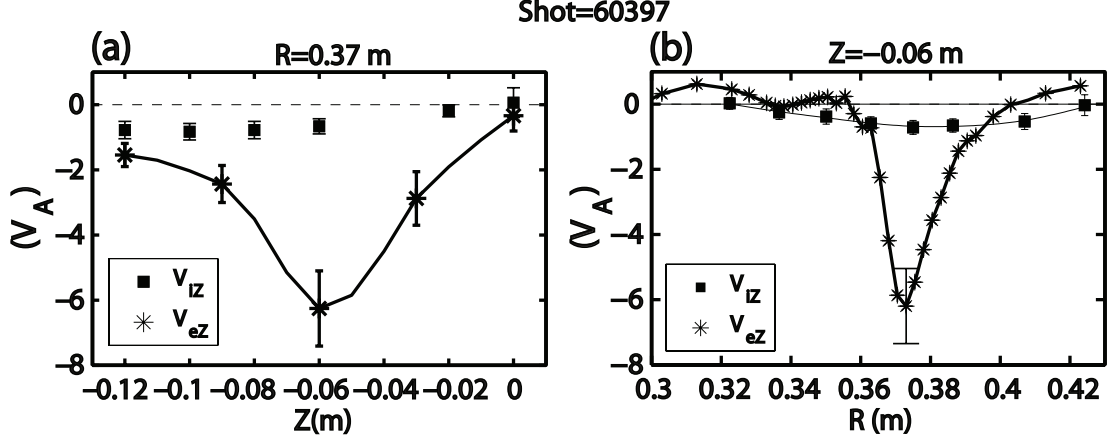
FIG. 12: The electron outflow velocity (V_{eZ}) in comparison with the ion outflow (V_{iz}) in a Helium plasma (fill pressure 8mTorr): (a) V_{eZ} (black asterisks) and V_{iZ} (black filled squares) versus Z along the current sheet center at $R = 0.38$ m; (b) V_{eZ} (black asterisks) and V_{iZ} (black filled squares) versus R across the current sheet at $Z = -0.06$ m. The error in the ion flow measurement is due to the time average and shot-to-shot variation. The electron outflow velocity is calculated from the in-plane current deduced from the QF measurement and from the ion outflow velocity using $V_{eZ} = -j_Z/(en_e) + V_{iZ}$. The error of the electron flow measurement comes from the density, magnetic field and ion outflow measurements.

the electron flow velocity scales with the ion Alfvén velocity. The scaling of the electron outflow velocity will be discussed in Section VI.

3. Comparison with the Ion Flow Measurement

In the previous analysis, it was assumed that the ions are moving much slower than the electrons. The assumption is reasonable because electrons are much lighter than any ion species, and are likely the current carriers. In order to justify this assumption and to reveal the characteristics of the ion outflow velocity, an axial Mach probe was used in the experiments to measure the ion outflow velocity (V_{iZ}).

Figure 12(a) plots the ion outflow velocity together with the calculated electron outflow velocity along the current sheet center, as a function of Z. It can be immediately seen that V_{eZ} everywhere is much larger than V_{iZ}. The maximum electron outflow velocity is about $6V_A$ and the maximum ion outflow velocity is only about $0.8V_A$. These two flows are not

24

only different in their peak value, but are also accelerated on different scales. The electron outflow velocity reaches its peak value about 0.06 m away from the X-line, while the ions are accelerated to the maximum velocity about 0.1 m away from the X-line. It is also clear that the electron outflow velocity decreases quickly after it peaks, and then approaches the ion outflow velocity. Presumably the two velocities will match each other, though this is not captured by the probe arrays in this discharge.

Figure 12(b) plots V_{eZ} and V_{iZ} as a function of R at $Z = -0.06$ m. The electron outflow region is the region where the electron outflow velocity is negative, and the ion outflow region is defined in the same way. It can be clearly seen that the ion outflow channel is much wider than the electron outflow region. In the region $R < 0.355$ m, the ions are already flowing away from the X-line ($V_{iZ} < 0$), while the electrons are still flowing towards the X-line since $V_{eZ} > 0$. This difference shows that the ions are demagnetized on a larger scale than the electrons, and do not need to flow into the narrow diffusion region as in the classical Sweet-Parker model. Thus, the reconnection rate greatly exceeds that predicted by the classical Sweet-Parker model. It can also been seen that in the downstream ($Z < -0.1$ m), the ion flow velocity can be comparable to the electron flow velocity. We note that although this similarity in the magnitude of the flow can contribute error to the electron flow velocity calculated from the in-plane current, the qualitative features of the in-plane electron flow pattern shown in Fig. 9 is not affected. Finally, we should point out that the error, which is contributed to the maximum electron outflow measurement by neglecting the ion outflow, is at most 20 percent.

C. The electron diffusion region

One important role of the Hall effect in magnetic reconnection is to modify the structure of the diffusion region. Instead of having a single diffusion region for both ions and electrons as in one-fluid MHD, the Hall-mediated fast reconnection has separate diffusion regions for the ions and electrons: an electron diffusion region is embedded in a broader ion diffusion region on the ion skin depth scale. Having directly demonstrated the separation of the electrons and ions close to the X-line, here we identify the electron diffusion region.

The electron diffusion region is identified by evaluating the generalized Ohm's law [52] across the reconnecting current sheet. Since the diagnostics shown in Fig. 1 measure the
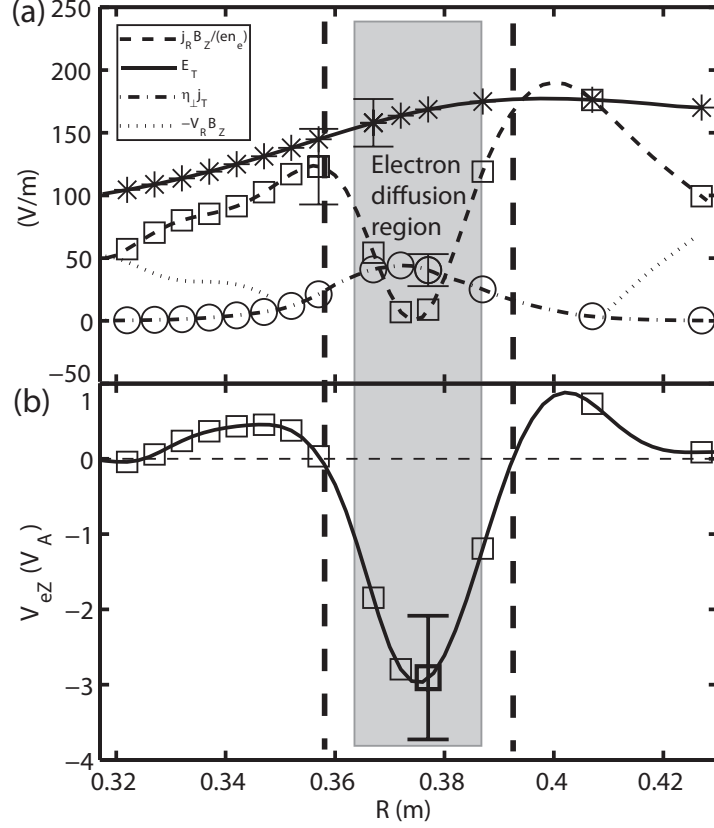
FIG. 13: (a) Radial profiles of four terms in the generalized Ohm's law: the reconnecting electric field (E_T) (solid line), the Hall term ($j_R B_Z/(en_e)$) (dashed line), the collisional resistive term ($\eta_\perp j_T$) (dash-dotted line), and $V_R B_Z$ (dotted line) in a Helium plasma (fill pressure=8 mTorr). The corresponding symbols show the coil positions. The error bars result from the uncertainties in the magnetic field, density and temperature measurements. All quantities are evaluated at $Z = -3$ cm. The shaded area denotes the the electron diffusion region, where $E_T + V_{eR} B_Z \neq 0$. (b) The radial profile of the electron outflow velocity V_{eZ} at $Z = -3$ cm, using the same horizontal axis as in (a). The shaded area shows the electron diffusion region identified in (a). The two vertical dashed lines denote the positions where $E_T - j_R B_Z/(en_e) \approx 0$.

equilibrium quantities, we perform a mean-field analysis of the generalized Ohm's law to separate the equilibrium and fluctuation components [53], and write down the toroidal component:

$$E_T + V_R B_Z = \eta_\perp j_T + \frac{j_R B_Z - j_Z B_R}{en_e} - \frac{m_e}{e} \frac{\partial V_{eT}}{\partial R} V_{eR} -$$
$$- \frac{1}{en_e} \left(\frac{\partial P_{eRT}}{\partial R} + \frac{\partial P_{eZT}}{\partial Z} \right) + \langle \cdots \rangle \tag{1}$$

26

where E_T is the reconnecting electric field, B_Z is the reconnecting magnetic field, V_R is the ion inflow velocity, $\eta_\perp$ is perpendicular Sptizer resistivity, j_T is the reconnecting current density, e is the electron charge, n_e is the plasma density, m_e is the electron mass, V_{eT} is the toroidal electron flow velocity, V_{eR} is the electron inflow velocity, $\mathbf{P}_e$ is the electron pressure tensor, and $\langle \cdots \rangle$ denotes all the fluctuation terms. Three terms are experimentally evaluated: E_T, $\eta_\perp j_T$ and $j_R B_Z/(e n_e)$. The reconnecting electric field is calculated from $E_T = \dot{\Psi}/2\pi R$ where Ψ is the poloidal flux function [38]. The reconnecting magnetic field B_Z is measured by the probe array at $Z = -3$ cm with a resolution up to 0.5 cm in the R direction. The j_T profile is calculated by fitting the measured reconnecting field to the Harris sheet profile [40]. Figure 13(a) plots the radial profiles of these terms. Since we do not have good B_R measurements close to the X-line, we are not able to evaluate the radial profile of the $j_Z B_R/(e n_e)$ term. However, since this term only peaks at the current sheet center due to the peaked profile of j_Z, we only need to estimate the magnitude of this term. The B_R at $Z = -6$ cm is about 30 G measured by a coarse magnetic probe array [20], we use the linearly interpolated value of 15 G as the estimate of B_R at $Z = -3$, noting that $B_R = 0$ at $Z = 0$. Thus we find that the magnitude of $j_Z B_R/(e n_e)$ is about 50 V/m in the current sheet center.

In Fig. 13(a), it is clear that far away from the current sheet center at $R \approx 37.5$ cm, the electron "frozen-in" condition, $E_T + V_{eR} B_Z = E_T + V_R B_Z - j_R B_Z/(e n_e) = 0$, must be satisfied, and thus $V_R B_Z$ is evaluated from $V_R B_Z = E_T - j_R B_Z/(e n_e)$. The resulting $V_R B_Z$ is positive, which shows that the ions are flowing towards the X-line, but the ion "frozen-in" condition is broken , since $E_T + V_R B_Z \neq 0$. This violation of the ion "frozen-in" condition shows this region is the ion diffusion region, although the boundaries of the ion diffusion region are beyond the measurement area. The two vertical dashed lines in Fig. 13(a) denote the positions where $E_T - j_R B_Z/(e n_e) \approx 0$, which demonstrates that the ions have been completely decoupled from the magnetic field lines since $V_R B_Z$ becomes much smaller than E_T, i.e. $V_R \ll E_T/B_Z$ where E_T/B_Z presents the velocity of the magnetic field lines. The shaded region between the dashed vertical lines is the electron diffusion region, where $(j_R B_Z - j_Z B_R)/(e n_e)$ becomes significantly less than E_T (note that the magnitude of $j_Z B_R/(e n_e)$ is about 50 V/m, much smaller than $E_T \approx 170$ V/m). Since $V_R \ll V_{eR}$ and $V_Z \ll V_{eZ}$ (shown in Fig. 12), where V_Z is the ion outflow velocity, this means that the electrons are decoupled from the magnetic field lines. It is obvious in Fig. 13(a) that the collisional

resistive term, $\eta_\perp \approx 40$ V/m, is not large enough to balance $E_T + j_Z B_R/(en_e)$, about 120 V/m, in the electron diffusion region. The magnitude of $(m_e/e)(\partial V_{eT}/\partial R)V_{eR}$ can be estimated as follows using typical numbers. We typically have $V_{eT} \sim 1 \times 10^5$ m/s, $\delta_{BZ} \sim 1$ cm and $V_{eR} \sim 1 \times 10^4$ m/s, where δ_{BZ} is the current sheet width. Thus $(m_e/e)(\partial V_{eT}/\partial R)V_{eR} \approx (m_e/e)V_{eT}/\delta_{BZ}V_{eR} \sim 1$ V/m, which is much smaller than the observed E_T (~ 170 V/m). Therefore the contribution from this electron inertia term can be neglected. The electron pressure term and the fluctuation terms, shown in Eqn. 1, can contribute to balance E_T, although the study of the exact roles of these terms is beyond the scope of this paper and will be addressed in an upcoming paper [54].

In Fig. 13(b) we plot the electron outflow velocity V_{eZ} as a function of R, where the two vertical lines and the electron diffusion region are extended from Fig. 13(a). It can be seen that, in Fig. 13(a), the two vertical lines are coincide with the edges of the electron outflow channel where the electrons flow toward the outflow region, i.e. $V_{eZ} < 0$. Thus we conclude that the width of the electron diffusion region is consistent with the width of the electron outflow channel, and we can use the following quantities of the electron outflow channel to characterize the electron diffusion region. The width of the electron outflow channel (δ_{BT}) is defined as the distance between the R position where the velocity peaks and the R position where the velocity decreases to 40 percent of its peak value. The definition is shown in Fig. 14. Note that although the out-of-plane current sheet structure agrees well with the Harris sheet equilibrium [40], there is still no theoretical model that quantitatively describes the structure of the electron outflow channel.

The length of the electron outflow region (L_{BT}) is defined as the distance along the current sheet center between the Z position where V_{eZ} peaks and the X-line, as shown in Fig. 11. This length characterizes the length of the electron acceleration region.

The value of δ_{BT} varies along Z. It seems difficult to characterize the electron outflow region using δ_{BT}. As briefly mentioned in Section IV, the electron outflow tends to converge when being accelerated. The self focusing effect can be readily explained by the mass conservation equation: $m_e n_e V_{eZ} \delta_{BT} \approx const$. When V_{eZ} increases δ_{BT} has to decrease to the conserve mass flux. The density profile along Z direction in the current sheet center is fairly uniform up to where V_{eZ} peaks (not shown). This implies that δ_{BT} can have a minimum along Z direction. Figure 15 (a) plots V_{eZ} as a function of Z, and V_{eZ} peaks at $Z = -6$ cm. Figure 15 (b) plots δ_{BT} against Z, which agrees with expectations: the minimum δ_{BT}
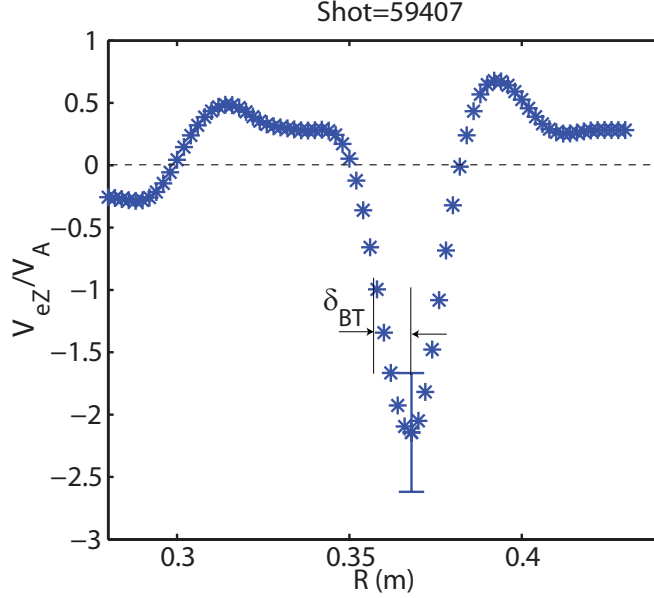
FIG. 14: The normalized electron outflow velocity (V_{eZ}) profile in R direction at Z=-6 cm in a Hydrogen plasma (fill pressure=2 mTorr). Definition of δ_{BT} is also shown.

corresponds to the maximum V_{eZ}. The missing data point at $Z = 0$ is because δ_{BT} is not well defined when V_{eZ} goes to zero close to the X-line. The value of δ_{BT} at the location of maximum V_{eZ} is well defined and unique in a single discharge. Thus, it can be used to characterize the spatial property of the electron outflow region along with L_{BT}. In the rest of this paper, δ_{BT} denotes this unique value of all δ_{BT}s.

Having identified the electron diffusion region, the scalings of its width of length can be studied by varying plasma density and ion species. Figure 16(a) plots δ_{BT} as a function of the electron skin depth (c/ω_{pe}). The error bars comes mainly from shot-to-shot variation. The data points with different ion species come together as one group, demonstrating that δ_{BT} scales only with the plasma density and have no dependence on the ion mass. The linear relation between δ_{BT} and the electron skin depth can be obtained from Fig. 16(a): $\delta_{BT} \approx 8c/\omega_{pe}$. This scaling of the electron diffusion region is consistent with numerical simulations [15, 16, 34–36, 54], although a different coefficient is found ($\delta_{BT} \approx$1-2c/ω_{pe}). In Fig. 16(b), L_{BT} is plotted as a function of c/ω_{pe}. It is clear that the data points with different ion species again come together, which shows that L_{BT} has no ion mass dependence, and is a function of the plasma density. For the Deuterium and Helium plasmas, L_{BT} tends to decrease as the plasma density is lowered. The same relationship is also present for

29
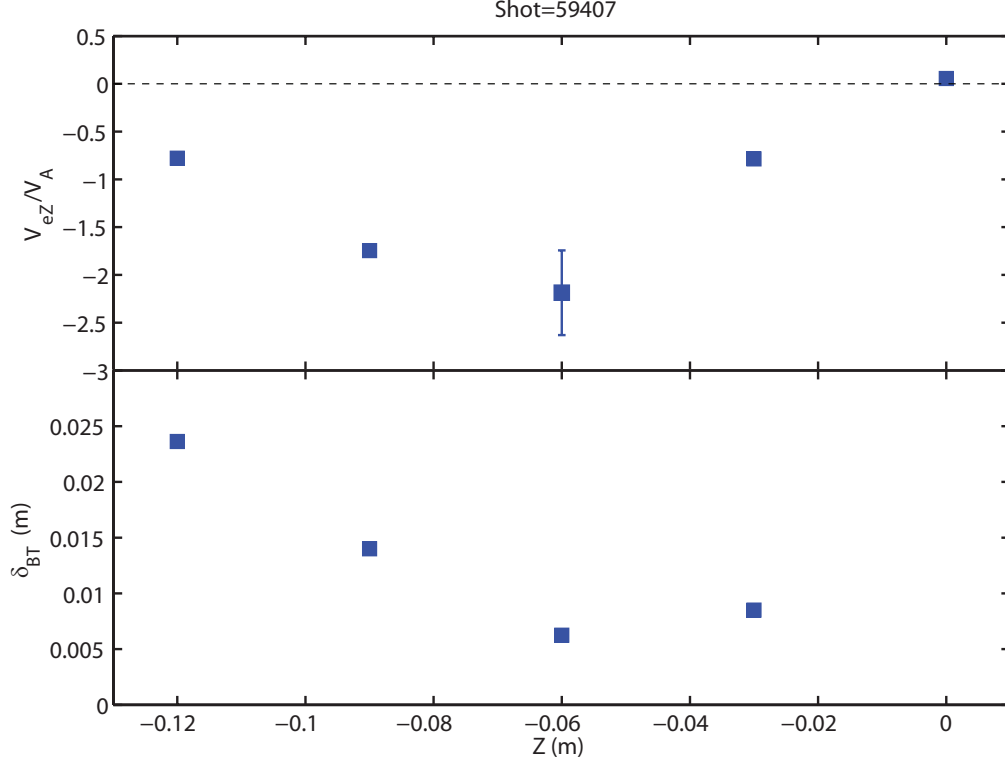
FIG. 15: (a) V_{eZ} versus Z; (b) δ_{BT} versus Z (δ_{BT} is not well defined if B_T is too small as close to the X-line) in a Hydrogen plasma (fill pressure=2 mTorr).

the Hydrogen plasmas, but is less clear because of the presence of large error bars. This relationship agrees with previous observations in MRX [55], where the current sheet length is found to decrease when fill pressure (plasma density) is lowered. The scaling of L_{BT} has been evaluated in a Hall-MHD simulation [15], where it was found that L_{BT} scales with the electron skin depth. While we have verified that L_{BT} does not depend on the ion mass, which agree with the simulation, we also find that L_{BT} ($\sim 40 - 80c/\omega_{pe}$) is not only much larger than $5c/\omega_{pe}$ as shown in the simulation [15], but does not scale with c/ω_{pe} either. The more recent numerical simulation [16, 56, 57] shows that the electron diffusion region can extend to tens of c/ω_{pi} in length when a large simulation domain (several hundred c/ω_{pi}) with either open or periodic boundary conditions. Note that L_{BT} is about 1-2c/ω_{pi} in the experiment, which is much less than tens of c/ω_{pi}. However, this difference could be due to the size of the experiment, *i.e.* the distance (40 cm) between two flux cores shown in Fig. 1 which corresponds to about $14c/\omega_{pi}$ in a high density hydrogen discharge. Note that even fewer c/ω_{pi} can fit in the experiment as the plasma density is lowered. The length of the

30
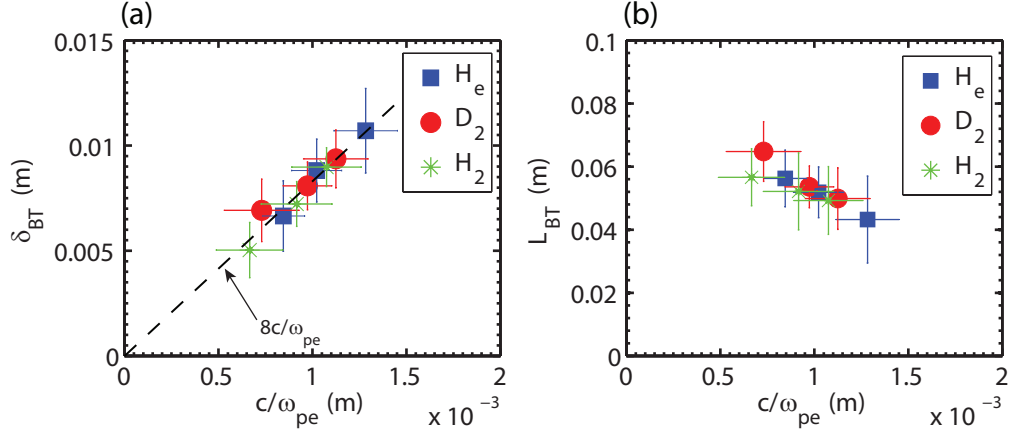
FIG. 16: (Color online) (a) δ_{BT} as a function of c/ω_{pe}; (b) L_{BT} as a function of c/ω_{pe}. c/ω_{pe} is calculated using the central density in the electron diffusion region. Discharges with three different ion species are shown: Helium (filled squares), Deuterium (filled circles) and Hydrogen (asterisks). The dashed line ($\delta_{BT} = 8c/\omega_{pe}$) is the linear best fit to the data. See text for the definitions of δ_{BT} and L_{BT}.

electron diffusion region will be addressed in future experiments where the distance between the flux cores will be varied. We note that the observed L_{BT} in the c/ω_{pe} unit is also much larger than $L_{BT} \sim 1.5 - 15c/\omega_{pe}$ obtained from the fully kinetic simulation of MRX for a range of parameters (mass ratios, initial densities and drive times) [35]. What causes this large difference is an open question and will be addressed in future detailed comparison between the experiment and simulation.

It should be noted that the definition of δ_{BT} in Ref. [15] is different from that in the experiment. In that simulation, δ_{BT} is defined as the distance from the point where the electron inflow deviates from the $\mathbf{E} \times \mathbf{B}$ drift. In the experiment, this definition is found difficult to apply due to experimental constraints[69]. The experimentally defined δ_{BT} characterizes the region where the electrons are decelerated in the R direction, diverted to and accelerated in the Z direction. Note that the δ_{BT} defined in the simulation also describes the same behavior of electrons. Thus the δ_{BT}s in the experiment and simulation are correlated with each other, and we conclude that δ_{BT} defined here also characterizes the width of the electron diffusion region. We also note that if we were able to apply the same definition of δ_{BT} in the experiment as in the simulation, the resulting δ_{BT} would be larger than $8c/\omega_{pe}$. However, in an upcoming paper with fully kinetic simulation (discussed in Section IV B),

δ_{BT} is about $1.6c/\omega_{pe}$ using the same definition as in the experiment [35].

VI. THE EFFECT OF DISSIPATION ON THE ELECTRON DIFFUSION RE-GION
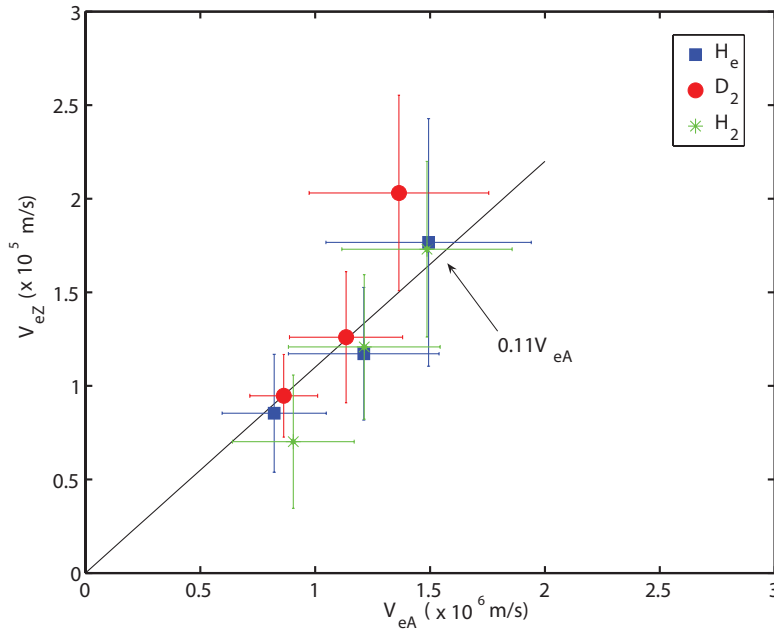
FIG. 17: (Color online) The maximum electron outflow velocity, V_{eZ}, as a function of the electron Alfvén velocity, V_{eA}, for plasmas of three different ion species: Hydrogen (green asterisks), Deuterium (red filled circles) and Helium (blue filled squares). The black solid line denotes $V_{eZ} = 0.11V_{eA}$, obtained from the linear fit to the data.

It has been shown in numerical simulations [15, 16, 37] that $V_{eZ} \approx V_{eA}$. However, we found the similar scaling but much smaller V_{eZ} in the experiment. Figure 17 plots the maximum electron outflow velocity as a function of the electron Alfvén velocity. The electron Alfvén velocity is calculated using the reconnecting magnetic field evaluated at the edge of the electron diffusion region, i.e. the reconnecting magnetic field at δ_{BT} away from the current sheet center. It is clear that V_{eZ} scales well with V_{eA} with a linear scaling: $V_{eZ} \approx 0.11V_{eA}$. It is also clear that V_{eZ} has no dependance on the ion mass since Fig. 17 shows similar relationship between V_{eZ} and V_{eA} for the plasmas with different ion species.

In a Hall-mediated reconnection, the following equation is satisfied:

$$\frac{V_{eZ}}{V_{eA}}\frac{\delta_{BT}}{c/\omega_{pe}} = 1 \tag{2}$$

where $V_{eA} = B_Z/\sqrt{\mu_0 n_e m_e}$ is the electron Alfvén velocity and c/ω_{pe} is the electron skin depth [11]. B_Z is the reconnecting magnetic field evaluated at the edge of the electron diffusion region. In this section a scaling that $\delta_{BT} \approx 8c/\omega_{pe}$ is found. We substitute this expression into Eqn. 2 and find that $V_{eZ}/V_{eA} \approx 0.125$ which agrees well with the approximate relationship obtained from Fig. 17: $V_{eZ} \approx 0.11V_{eA}$. This agreement shows that Eqn. 2, based on the balance between the generation and convection of the out-of-plane field, captures the basic physics in the ion diffusion region. We can apply the Sweet-Parker analysis [2, 7] to the electron diffusion region. Note that we assume the density profile is smooth in the electron diffusion region. Similar to the result of Sweet-Parker model that the ion outflow from the ion diffusion region is the ion Alfvén velocity, the electron outflow velocity from the electron diffusion region should be the electron Alfvén velocity, $V_{eZ} = V_{eA}$. This expression clearly provides a constraint to Eqn. 2, so that we have: $\delta_{BT} = c/\omega_{pe}$. This scaling for δ_{BT} is consistent with numerical simulation [15]. On the other hand, we have found a different scaling in MRX: $\delta_{BT} \approx 8c/\omega_{pe}$ with $V_{eZ} \approx 0.11V_{eA}$. The difference apparently comes from the fact that the electron outflow velocity in MRX is only $0.11V_{eA}$, much smaller than the electron Alfvén velocity predicted by the Sweet-Parker-type analysis and numerical simulations.

In order to explain this discrepancy, we consider the Z component of the steady-state electron momentum equation:

$$m_e n_e V_{eZ}\frac{\partial V_{eZ}}{\partial Z} = \frac{1}{\mu_0}B_R\frac{\partial B_Z}{\partial R} - \frac{1}{\mu_0}B_R\frac{\partial B_R}{\partial Z} - m_e n_e \nu_{ei} V_{eZ} \tag{3}$$

where the MRX coordinate system is used and we assumed that $V_{iZ} \ll V_{eZ}$, a reasonable assumption inside in the electron diffusion region; ν_{ei} is the electron-ion collision frequency. Note that the electron density and temperature profiles in the electron diffusion region show small variance (not shown) along the Z direction. Thus, the electron pressure gradient term is neglected in Eqn. 3 (We note that the pressure term can be important in numerical simulation [35]). We also, for now, neglect E_Z, which will be discussed later. We integrate Eqn. 3 from $Z = 0$ (the X-line) to $Z = L_{BT}$ (the edge of the electron diffusion region):

$$\frac{1}{2}m_e n_e V_{eZ}^2 = \frac{B_R L_{BT}}{2\mu_0}\frac{B_Z}{\delta_{BT}} - \frac{B_R^2}{2\mu_0} - m_e n_e \nu_{ei}\frac{V_{eZ}L_{BT}}{2} \tag{4}$$

33

where we used $\partial/\partial R \sim 1/\delta_{BT}$; B_R and V_{eZ} are linear functions of Z; B_Z is independent of Z. All the quantities in Eqn. 4 are evaluated at the edge of the electron diffusion region. Due to the assumptions of steady state, incompressibility and broad density profile in the R direction, we have:

$$E_T = V_{eZ}B_R = V_{eR}B_Z \tag{5}$$

$$V_{eR}L_{BT} = V_{eZ}\delta_{BT} \tag{6}$$

Using above equations we have $B_R L_{BT} = B_Z \delta_{BT}$, and substituting this equality into Eqn. 4 yields:

$$\frac{1}{2}m_e n_e V_{eZ}^2 = \frac{B_Z^2}{2\mu_0} - m_e n_e \nu_{ei}\frac{V_{eZ}L_{BT}}{2} \tag{7}$$

where we have used $B_R^2 \ll B_Z^2$, well satisfied because $\delta_{BT}^2/L_{BT}^2 \ll 1$. It is easy to see that without the last term on the right-hand side (RHS), the electron out flow velocity would be the electron Alfvén velocity $V_{eA} = B_Z/\sqrt{\mu_0 m_e n_e}$. Thus the last term on the RHS is a dissipation term which slows the electron outflow. Let us then rewrite this term as

$$m_e n_e \nu_{ei}\frac{V_{eZ}L_{BT}}{2} = \frac{B_Z^2}{2\mu_0}\frac{V_{eZ}V_{e,th}L_{BT}}{V_{eA}^2\lambda_{mfp}} = \frac{B_Z^2}{2\mu_0}\frac{V_{eZ}}{V_{eA}}A \tag{8}$$

where $V_{e,th} = \sqrt{kT_e/m_e}$ is the electron thermal velocity, $\lambda_{mpf} = V_{e,th}/\nu_{ei}$ is the electron mean free path and $A = V_{e,th}/V_{eA} \times L_{BT}/\lambda_{mfp}$. We then substitute Eqn. 8 back into Eqn. 7:

$$\frac{V_{eZ}^2}{V_{eA}^2} = 1 - A\frac{V_{eZ}}{V_{eA}} \tag{9}$$

We solve Eqn. 9 for V_{eZ}/V_{eA}:

$$\frac{V_{eZ}}{V_{eA}} = \frac{-A + \sqrt{A^2 + 4}}{2} \tag{10}$$

where A can be evaluated from experimental parameters, allowing V_{eZ}/V_{eA} to be estimated independently from the in-plane electron flow measurement.

Before evaluating Eqn. 10 experimentally, we can examine its asymptotic behavior in the limits of $A^2 \ll 4$ and $A^2 \gg 4$. In the first limit (meaning that the friction force on the electrons is much less than the magnetic tension force), Eqn. 10 becomes $V_{eZ}/V_{eA} = 1 - A/2$. With no friction force, $A = 0$, the electron outflow equals the electron Alfvén velocity, as expected. With a small friction force, V_{eZ}/V_{eA} decreases linearly as a function of A. In the $A^2 \gg 4$ limit (meaning that the friction force is comparable to the magnetic tension force), Eqn. 10 becomes: $V_{eZ}/V_{eA} = 1/A$. As $A \to \infty$, V_{eZ}/V_{eA} approaches zero, as expected since
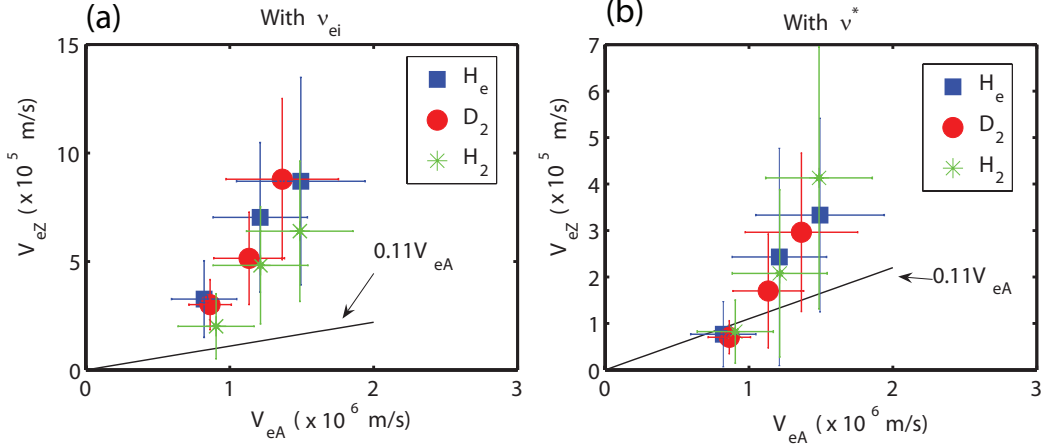
FIG. 18: (Color online) (a) The electron out flow velocity V_{eZ}, estimated using the classical electron-ion collision frequency, versus the electron Alfvén velocity; (b) The electron out flow velocity V_{eZ}, estimated using the effective collision frequency, versus the electron Alfvén velocity. The black solid lines in both panels denote $V_{eZ} = 0.11V_{eA}$, obtained from the linear fit to the data.

the friction force slows down the electron outflow. This limit is what we are most interested in, since we want to explain the observed slower electron outflow. The electron outflow in this limit can be written as:

$$\frac{V_{eZ}}{V_{eA}} = \frac{1}{A} = \frac{\lambda_{mfp}}{L_{BT}}\frac{V_{eA}}{V_{e,th}} \tag{11}$$

We can then estimate V_{eZ}/V_{eA} using typical MRX parameters. In MRX, we have $V_{eA} \sim V_{e,th}$ from force balance in the R direction. Thus, Eqn. 11 is simplified as $V_{eZ}/V_{eA} \sim \lambda_{mfp}/L_{BT}$, and a smaller λ_{mfp} leads to a smaller electron outflow.

For collisionless Hydrogen plasmas, the typical λ_{mfp} from Coulomb electron-ion collisions is about 0.02 m, and the typical L_{BT} is about 0.05 m. Thus we have $A = 2.5$, which does not satisfy $A^2 \gg 4$. Then we must use Eqn. 10, which gives an outflow velocity of $0.35V_{eA}$. This is still much larger than the observed $0.11V_{eA}$. We then use the effective collision rate, ν^*, observed in MRX[70]. The typical anomalous factor in Hydrogen discharges is about three, thus the effective λ_{mfp} is decreased by a factor of three, and $A = 7.5$, satisfying $A^2 \gg 4$. Then we have $V_{eZ} \sim 0.13V_{eA}$, close to the observed value, $V_{eZ} \approx 0.11V_{eA}$. Thus, in order to explain the observed electron outflow, anomalous collisions must be taken into account.

The experimentally estimated V_{eZ}, based on Eqn. 10, is plotted as a function of V_{eA} in Fig. 18. In Fig. 18(a) V_{eZ} is estimated utilizing the classical electron-ion collision frequency.

We can see the electron outflow is about $0.3 - 0.6V_{eA}$, which still deviates from what is observed, $0.11V_{eA}$. In Fig. 18(b), the effective collision rate is used in the estimate. The anomalous collisions successfully reduce the electron outflow to the $0.1-0.3V_{eA}$ range, which agrees fairly well with the measurement, $V_{eZ} \approx 0.11V_{eA}$, given the simplicity of the estimate. It clearly shows that the electron outflow channel can be broadened by collisions, and the origin of the anomalous collisions is still under investigation. Note that in Fig. 18(b), the estimated V_{eZ} can still be twice larger than the experimental expression, $V_{eZ} \approx 0.11V_{eA}$. Thus additional effects can still contribute to the slow-down of the electrons. One possible candidate is the in-plane electrostatic electric field pointing away from the X-line in the Z direction [58], which, if present, slows down the electron outflow. The measurement of this electric field is a subject of the future work in MRX. The electron pressure gradient in the Z direction could also slow the electron outflow. Within the present uncertainty in the electron pressure measurement, the pressure gradient seems small. However, more precise measurements are required to fully evaluate the contribution from the pressure gradient.

We find here that the effective collision rate not only limits the reconnecting current density, but also plays an important role in limiting the electron outflow velocity in the electron diffusion region. This relationship can be understood as follows. The electrons in the electron diffusion region drift in both the Z and toroidal (or out-of-plane) directions. In steady state, the friction force from the effective collisions are in the opposite direction to the drift motion. This friction force can be projected to both the Z and toroidal directions, so that the same anomalous factor should be used in both directions.

We note that although the electron outflow cannot reach the electron Alfvén velocity, the outflow channel is also broadened. Thus the total electron outflow flux is conserved since $V_{eZ}/V_{eA} \times \delta_{BT}/(c/\omega_{pe}) = 1$ is still approximately satisfied. This suggests that the total electron outflow flux is independent of the width of the electron diffusion region, which is one of the reasons why the Hall effect can facilitate fast magnetic reconnection [11]. Therefore our experiment is consistent with the Hall-mediated fast reconnection scenario [14].

Note that in the experiment, changing the plasma density not only changes the electron dynamics but also affects the ion dynamics, which may control the reconnection rate as suggested in numerical simulations [13–15]. This may explain why MRX does not have a constant reconnection rate (conventionally defined as the ratio between the plasma inflow velocity and the ion Alfvén velocity at the ion diffusion region edge) as in numerical simulation

[15, 59], even though the Hall effect is present in MRX. In order to determine the reconnection rate at the electron diffusion region, we rewrite Eqn. 2 using $L_{BT}V_{eR} = \delta_{BT}V_e eZ$ (mass conservation equation in the electron diffusion region):

$$\frac{V_{eR}}{V_{eA}} = \frac{c/\omega_{pe}}{L_{BT}} \tag{12}$$

We can see that the reconnection rate is now controlled by L_{BT}. As shown in numerical simulations [15, 59], L_{BT} scales with c/ω_{pe}, which yields a constant reconnection rate. On the other hand, in the experiment, L_{BT} more likely scales inversely with c/ω_{pe}, as shown in Fig. 16(b). The reconnection rate is thus higher when the plasma density is lowered, which is consistent with previous MRX results [38].

We note that electron diffusion regions having an average thickness of $0.3c/\omega_{pe}$ were observed near the subsolar magnetopause [27], where the classical resistivity is ignorable. Since the electron diffusion region is identified close to the X-line in the experiment, we do not know how our observation is directly related to the above observation where the electron diffusion region was observed away from the X-line. However, we could argue that individual electron regions of the small size could bunch together in a larger region of several c/ω_{pe}, which may explain the measured $\delta_{BT} \approx 8c/\omega_{pe}$ in the experiment. But the magnetic probe arrays used in the experiment do not have the resolution to verify this interpretation.

VII. SUMMARY

In this paper, we presented a detailed experimental study of the Hall effect, which was identified to facilitate fast reconnection in 2D numerical simulations [14]. The study of the Hall effect was conducted by experimentally measuring the quadrupole out-of-plane magnetic field (QF) generated during magnetic reconnection in MRX. This QF, predicted conceptually by Sonnerup [45] and observed in many numerical simulations [11, 12, 34, 43], is the most significant signature of the Hall effect during non-guide-field reconnection.

The QF was measured by using both a coarse-resolution 2D magnetic probe array [20] and another set of five linear magnetic probe arrays with higher resolution. The measured out-of-plane field clearly shows the quadrupole-type configuration with its field reversal in the current sheet center, which agrees with numerical simulations. Time-resolved measurements show that even though the QF evolution in MRX is affected by the toroidal field generated

by the external coils, the fully developed QF is independent of how the TF coils are driven. We showed that the QF can last for more than 10 Alfvén times.

We compared the measured QF with theoretical models. A plot of the QF strength along radial rays pointing away from the X-line shows both agreement and deviation from the Uzdensky-Kulsrud model [46], and illustrates the deviation of the measured diffusion region from the simple X-point type. We calculated the in-plane current density from the out-of-plane field measurement, using Ampere's law. The in-plane current shows large-scale field-aligned component, in good agreement with the Uzdensky-Kulsrud model. The measured QF, with different ion species, were compared with the QF from a numerical simulation. The basic features of the QF were found to be consistent with the numerical simulation. We found a method to identify the separatrices by tracing the ridges of the QF, which can be used to find the separatrices without measuring the in-plane magnetic field.

The roles of the Hall effect in magnetic reconnection were explored. The calculated in-plane electron flow pattern shows remarkable agreement with that in a numerical simulation. This indicates that the ions are moving differently from the electrons, as shown in the numerical simulation. The electron inflow is deduced by the combination of the $E \times B$ drift and in-plane current measurement. It shows that the reconnection rate (V_{in}/V_A) is about 0.2, which agrees with numerical simulation [21]. We found that the electron outflow velocity is super-Alfvénic ($\sim 2V_A$), in agreement with many numerical simulations [13, 34, 60–65]. The super-Alfvénic electron outflow is a central point in Hall-mediated fast reconnection. By exceeding the ion Alfvén velocity, the limit on the outflow velocity in the Sweet-Parker model, the electrons are much less constrained by the width of the outflow channel. This property allows the dissipation to operate strongly at a scale smaller than the ion diffusion region, but still to pose no limit on the electron mass flow.

The ion outflow was measured with a Mach probe. It was shown that the maximum ion outflow velocity is much slower than the maximum electron out flow velocity, and the ion outflow channel is much wider than then electron outflow channel. This observation immediately supports the role of the Hall effect in fast reconnection: by decoupling ions from electrons on a larger spatial scale, the ion outflow channel is no longer controlled by the dissipative mechanism around the X-line. Thus, the mass flow constraint, present in the Sweet-Parker model, does not limit reconnection in the presence of the Hall effect.

The measurement of the in-plane electron flow allowed us to identify the electron diffusion

region as the electron outflow channel, where the electrons are accelerated to high speed in this narrow outflow channel. Its width, δ_{BT}, is defined as the distance between the location where the outflow velocity peaks and the location where it drops to 40 percent of the peak value. The value of δ_{BT} at the location of the peak electron outflow velocity was used to characterize the electron outflow channel. We found a scaling law for this width, $\delta_{BT} \approx 8c/\omega_{pe}$, from a large number of discharges with different density and ion species. The independence of this width on the ion mass shows the electron outflow channel is controlled by the electron dynamics alone, in good agreement with numerical simulations [15, 34, 37]. A correlation between the length of the electron diffusion region (L_{BT}) and the electron skin depth was also presented. It is clear that L_{BT} has no dependance on the ion mass, and thus does not scale with the ion skin depth. Furthermore, L_{BT} was found to decrease as the plasma density is lowered, although it is unclear with what kind of functional form because large errors are present.

The electron outflow velocity is found to scale with the electron Alfvén velocity, where the magnetic field is evaluated at the edge of the electron diffusion region: $V_{eZ} \approx 0.11V_{eA}$. This scaling, combined with the scaling for δ_{BT}, shows good agreement with the analytical analysis of the Hall effect [11]. However, the observed electron outflow ($0.11V_{eA}$) is much slower than theoretical prediction (V_{eA}). We demonstrate that, by employing friction force from classical and anomalous collisions in the electron momentum equation, the observed electron outflow velocity can be qualitatively explained. We note that although the electron outflow cannot reach the electron Alfvén velocity as in simulations, the outflow channel is broadened and the total electron outflow flux is still conserved. Thus, the experimental result is consistent with the Hall-mediated fast reconnection scenario.

Acknowledgments

---

[1] J. W. Dungey, Phys. Rev. Lett. **6**, 47 (1961).

[2] P. A. Sweet, *The Neutral Point Theory of Solar Flares* (Cambridge Univeristy Press, Cambridge, Britain, 1958).

[3] J. B. Taylor, Rev. Mod. Phys. **58**, 741 (1986).

[4] J. Sarff, A. Almagri, J. Anderson1, T. Biewer, A. Blair, M. Cengher, B. Chapman, P. Chattopadhyay, D. Craig, D. D. Hartog, F. Ebrahimi, G. Fiksel, C. B. Forest, J. A. Goetz, D. Holly, B. Hudson, T. W. Lovell, K. J. McCollam, P. D. Nonn, R. O'Connell, S. P. Oliva, S. C. Prager, J. C. Reardon, M. A. Thomas, M. D. Wyman, D. L. Brower, W. X. Ding, S. D. Terry, M. D. Carter, V. I. Davydenko, A. A. Ivanov, R. W. Harvey, R. I. Pinsker, C. Xiao, Nuclear Fusion **43**, 1684 (2003).

[5] S. V. Goeler, W. Stodiek, and N. Sauthoff, Phys. Rev. Lett. **33**, 1201 (1974).

[6] M. Yamada, F. M. Levinton, N. Pomphrey, R. Budhy, J. Manickam, and Y. Nagayama, Phys. Plasmas **1**, 3269 (1994).

[7] E. N. Parker, J. Geophys. Res. **62**, 1957 (1957).

[8] H. E. Petschek, NASA Spec. Pub. SP-50 p. 425 (1964).

[9] R. Kulsrud, Earth Planets Space **53**, 417 (2001).

[10] D. Biskamp, Phys. Fluids **29**, 1520 (1986).

[11] M. E. Mandt, R. E. Denton, and J. F. Drake, Geophys. Res. Lett. **21**, 73 (1994).

[12] M. A. Shay and J. F. Drake, Geophys. Res. Lett. **25**, 3759 (1998).

[13] M. Hesse, K. Schindler, J. Birn, and M. Kuznetsova, Phys. Plasmas **6**, 1781 (1999).

[14] J. Birn and et al., J. Geophys. Res. **106**, 3715 (2001).

[15] M. A. Shay, J. F. Drake, B. N. Rogers, and R. E. Denton, J. Geophys. Res. **106**, 3759 (2001).

[16] W. Daughton, J. Scudder, and H. Karimabadi, Phys. Plasmas **13**, 072101 (2006).

[17] X. H. Deng and H. Matsumoto, Nature **410**, 557 (2001).

[18] M. Oieroset, T. D. Phan, M. Fujimoto, R. P. Lin, and R. P. Lepping, Nature **412**, 414 (2001).

[19] F. S. Mozer, S. D. Bale, and T. D. Phan, Phys. Rev. Lett. **89**, 015002 (2002).

[20] Y. Ren, M. Yamada, S. Gerhardt, H. Ji, R. Kulsrud, and A. Kuritsyn, Phys. Rev. Lett. **95**, 055003 (2005).

[21] M. Yamada, Y. Ren, H. Ji, J. Breslau, S. Gerhardt, R. Kulsrud, and A. Kuritsyn, Phys. Plasmas **15**, 052119 (2006).

[22] M. R. Brown, C. D. Cothran, and J. Fung, Phys. Plasmas **13**, 056503 (2006).

[23] F. S. Mozer, V. Angelopoulos, J. Bonnell, K. H. Glassmeier, and J. McFadden, Geophys. Res. Lett. **In press** (2008).

[24] J. D. Scudder, F. S. Mozer, N. C. Maynard, and C. T. Russell, J. Geophys. Res. **107**, 1294 (2002).

[25] F. S. Mozer, S. D. Bale, T. D. Phan, and J. A. Osborne, Phys. Rev. Lett. **91**, 245002 (2003).

[26] F. S. Mozer, J. Geophys. Res. **110**, A12222 (2005).

[27] F. S. Mozer, S. D. Bale, J. P. McFadden, and R. B. Torbert, Geophys. Res. Lett. **32**, L24102 (2005).

[28] J. R. Wygant, C. A. Cattell, R. Lysak, Y. Song, J. Dombeck, J. McFadden, F. S. Mozer, C. W. Carlson, G. Parks, E. A. Lucek, et al., J. Geophys. Res. **110**, L03105 (2005).

[29] T. D. Phan, J. F. Drake, M. A. Shay, F. S. Mozer, and J. P. Eastwood, Phys. Rev. Lett. **99**, 255002 (2007).

[30] R. L. Stenzel and W. Gekeman, Phys. Rev. Lett. **42**, 1055 (1979).

[31] J. Egedal, A. Fasoli, and J. Nazemi, Phys. Rev. Lett. **90**, 135003 (2003).

[32] Y. Ren, Ph.D. thesis, Princeton Univ. (2007).

[33] Y. Ren, M. Yamada, H. Ji, S. P. Gerhardt, and R. Kulsrud, submitted to Phys. Rev. Lett. (2008).

[34] P. L. Pritchett, J. Geophys. Res. **106**, 3783 (2001).

[35] S. Dorfman, W. Daughton, and V. Roytershteyn, to be submitted to Phys. Plasmas (unpublished).

[36] D. Biskamp, E. Schwarz, and J. F. Drake, Phys. Rev. Lett. **75**, 3850 (1995).

[37] M. Hoshino, T. Mukai, T. Terasawa, and I. Shinohara, J. Geophys. Res. **106**, 25979 (2001).

[38] H. Ji, M. Yamada, S. Hsu, and R. Kulsrud, Phys. Rev. Lett. **80**, 3256 (1998).

[39] H. Ji, M. Yamada, S. Hsu, R. Kulsrud, T. Carter, and S. Zaharia, Phys. Plasmas **6**, 1743 (1999).

[40] M. Yamada, H. Ji, S. Hsu, T. Carter, R. Kulsrud, and F. Trintchouk, Phys. Plasmas **7**, 1781 (2000).

[41] M. Yamada, H. Ji, S. Hsu, T. Carter, R. Kulsrud, Y. Ono, and F. Perkins, Phys. Plasmas **4**,

1936 (1997).

[42] M. Yamada, H. P. Furth, W. Hsu, A. Janos, S. Jardin, M. Okabayashi, J. Sinnis, T. H. Stix, and K. Yamazaki, Phys. Rev. Lett. **46**, 188 (1981).

[43] P. Ricci, J. U. Brackbill, W. Daughton, and G. Lapenta, Phys. Plasmas **1**, 4102 (2004).

[44] F. S. Mozer, *Private communication* (2006).

[45] B. U. Ö. Sonnerup, *Solar System Plasma Physics* (North-Holland, New York, 1979), vol. 3, chap. Magneti Field Reconnection, p. 45.

[46] D. A. Uzdensky and R. M. Kulsrud, Phys. Plasmas **13**, 062305 (2006).

[47] T. Nagai, I. Shinohara, M. Fujimoto, H. Hoshino, Y. Saito, S. Machida, and T. Mukai, J. Geophys. Res. **106**, 25929 (2001).

[48] J. A. Breslau and S. C. Jardin, Phys. Plasmas **10**, 1291 (2003).

[49] S. D. Bale, F. S. Mozer, and T. Phan, Geophys. Res. Lett. **29**, 2180 (2002).

[50] A. Kuritsyn, Ph.D. thesis, Princeton University (2005).

[51] N. A. Murphy and C. R. Sovinec, to be published in Phys. Plasmas (2008).

[52] D. Biskamp, *Magnetic Reconnection in Plasmas* (Cambridge University Press, Cambridge, Britain, 2000).

[53] F. Krause and K. H. Rädler, *Mean-field magnetohydrodynamics and dynamo theory* (Pergamon Press, Oxford ; New York, 1980), 1st ed.

[54] H. Ji, Y. Ren, M. Yamada, S. Dorfman, W. Daughton, and S. Gerhardt, to be submitted to Geophy. Res. Lett. (2008).

[55] A. Kuritsyn, H. Ji, S. Gerhardt, Y. Ren, and M. Yamada, Geophys. Res. Lett. **34**, L16106 (2007).

[56] M. A. Shay, J. F. Drake, and M. Swisdak, Phys. Rev. Lett. **99**, 155002 (2007).

[57] K. Fujimoto, Phys. Plasmas **13**, 2904 (2006).

[58] P. L. Pritchett, J. Geophys. Res. **110**, A01209 (2005).

[59] M. A. Shay, J. F. Drake, B. N. Rogers, and R. E. Denton, Geophys. Res. Lett. **26**, 2163 (1999).

[60] Z. Ma and A. Bhattacharjee, J. Geophys. Res. **106**, 3773 (2001).

[61] M. Hesse, J. Birn, and M. Kuznetsova, J. Geophys. Res. **106**, 3721 (2001).

[62] J. A. Breslau, Ph.D. thesis, Princeton Univ. (2001).

[63] S. P. Jin, H. A. Yang, and X. G. Wang, Phys. Plasmas **12**, 042902 (2005).

[64] M. A. Shay, J. F. Drake, R. E. Denton, and D. Biskamp, J. Geophys. Res. **103**, 9165 (1998).

[65] P. L. Pritchett, J. Geophys. Res. **106**, 25961 (2001).

[66] Reconnecting magnetic field and plasma density are approximately symmetric across the neutral sheet

[67] The out-of-plane current density can be calculated as $(\partial B_Z/\partial R - \partial B_R/\partial Z)/\mu_0$, but we do not have a detailed B_R measurement to evaluate $\partial B_R/\partial Z$.

[68] V_{eR} cannot be accurately calculated at $Z = 0$ cm, the X-line, due to a lack of measurements at $Z > 0$ cm.

[69] It requires an accurate density profile across current sheet for each discharge, which we do not have the capability to measure, and the measurement of the electron inflow V_{eR} is less accurate than the measurement of V_{eZ}.

[70] The effective collision rate used is deduced from the resistivity enhancement, $\nu^*/\nu_{ei} = E_T/j_T/\eta_{Spitzer}$, where E_T is the reconnecting electric field at the current sheet center and j_T is the reconnecting current density. ν^* represents both anomalous and classical collisions.